Master's thesis

NTNU
Norwegian University of Science and Technology
Faculty of Information Technology and Electrical Engineering
Department of Electronic Systems

Christopher Frøseth Amundsen

Fabrication and Characterisation of an on-chip Microheater for artificial spin ices

Master's thesis in Electronics Systems Design and Innovation
Supervisor: Erik Folven
Co-supervisor: Ida Breivik and Alv Skarpeid
June 2023

NTNU
Norwegian University of
Science and Technology

Christopher Frøseth Amundsen

Fabrication and Characterisation of an on-chip Microheater for artificial spin ices

Master's thesis in Electronics Systems Design and Innovation
Supervisor: Erik Folven
Co-supervisor: Ida Breivik and Alv Skarpeid
June 2023

Norwegian University of Science and Technology
Faculty of Information Technology and Electrical Engineering
Department of Electronic Systems

Abstract

Artificial spin ice (ASI) is a magnetic metamaterial which consists of interacting nanomagnets arranged in various geometries. Such ASI ensembles exhibit complex dynamics and may be utilized in computing [1]. Temperature is an important parameter to control in ASIs as it dictates the complicity and characteristics of the system [2]. The temperature characterisation of ASIs requires further exploration and is significant for a deeper understanding of these systems [3]. In this thesis, we have developed and characterised an on-chip microheater designed for thermal characterisation of ASI systems. The microheater design is based on ohmic heating and consists of a heater and a thermometer, surrounding an area where ASI structures may be placed. The fabrication of the microheater involved photolithography, metalization, and lift-off. Both gold and copper microheaters were successfully fabricated and the temperature coefficients for the thin films were obtained experimentally. In addition, a test chamber provided precise control of the microheater, thereby allowing us to increase and regulate the temperature. The result is a microheater surrounding ASIs capable of heating ASIs accurately from room temperature up to 130 °C. Future work involves further characterisation of the microheater, creating a feedback system which provides a stable temperature and optimize the test chamber such that it can utilized by instruments capable of observing magnetic contrasts.

Sammendrag

Kunstige spinnis er et magnetisk metamateriale som består av vekselvirkende nanomagneter arrangert i spesielle geometrier. Slike systemer har kompleks dynamikk og egenskaper man ofte ser i databehandlingssystemer [1]. Temperatur er en viktig parameter for å kontrollere kunstige spinnis systemer ettersom det kontrollerer egenskapene til systemet [2]. For å få en dypere forståelse av kunstige spinnis kreves det ytterligere forskning og temperaturkarakterisering av kusntig spinnis er en viktig del av dette [3]. I denne oppgaven har vi utviklet og karakterisert en mikrovarmer designet for termisk kontrol av kunstige spinnis. Designet er basert på ohmsk oppvarming og består av en varmer og et termometer som omgir et område hvor spinnis kan plasseres. Fabrikasjonen av mikrovarmeren involverte fotolitografi og metallisering. Både gull- og kobbermikrovarmere ble fabrikert og temperaturkoeffisientene ble funnet eksprimentelt. Videre brukte vi et testkammer for å kontrollere mikrovarmeren slik at temperaturen kunne reguleres. Resultatet er en mikrovarmer som kan øke temperaturen til spinnis systemenes nøyaktig fra romtemperatur og opp til 130 °C. Fremtidig arbeid innebærer ytterligere karakterisering av mikrovarmeren, skape et tilbakekoblingssystem som justere strømmen i sanntid og optimerer testkammeret slik at det er kompatibelt med instrumenter som er i stand til å observere magnetiske kontraster.

Chapter 1

Preface

The thesis is the final project of a five-year Master's Degree Program in Electronics Systems Design and Innovation with a specialization in nanoelectronics and photonics at the Norwegian University of Science and Technology. The work was done during the spring semester of 2023 with the Department of Electronics (IES). During the fall 2022 semester, a specialization project was done which resulted in the creation of a microheater using photolitography, metalization and lift-off. In this thesis, parts of the theory chapters were written during the specialization project and are included as they still are relevant.

Acknowledgements
To begin with, I would like to thank my supervisors Erik Folven, Ida Breivik and Alv Skarpeid for the past two semesters. They have contributed with valuable discussions, guidance and significant assistance through weekly meetings for the past year. I would especially like to thank Ida Breivik and Alv Skarpeid for fabricating samples when I did not have the required training, proofreading a lot of drafts and always keeping their office open whenever I needed help.
I would also like to thank all of the friends I have made throughout my years at NTNU. The time at NTNU would not be the same without you. In addition, I would like to thank my family for always supporting me and provide help whenever it was needed. Especially my father who have helped with proofreading and valuable discussion whenever I have asked.

Contents

Chapter 2

Introduction

The transistor has been one of the most important inventions in recent history as it is the foundation for most electrical devices, including computers. The size of the transistors has been reduced rapidly in pace with Moores Law [4], to create more powerful devices with lower power consumption. The need for computational power is expected to keep growing but we are approaching a threshold as further reduction of the transistor size and their power consumption are becoming increasingly challenging [5]. Exploring alternative computational paradigms is therefore an important field of research.

Nanomagnetic devices are promising as they have the potential to give us computational devices with significantly lower power consumption compared to transistor-based counterparts. A bistable nanomagnet has two magnetization states and can create bits represented by magnetization instead of voltage. When nanomagnets are arranged close together, their magnetic fields will interact and the behaviour becomes complicated. To achieve a better understanding of the nanomagnets' potential, researches are experimenting how these complicated magnetic interactions can be utilized. Artificial spin ices (ASIs) is magnetic metamaterials consisting of nanomagnets and the collective behaviour of ASIs exhibits properties that may be used in computing and artificial intelligence [1]. The geometry of ASIs deliberately introduce geometrical frustration [3], meaning the system is not able to energetically satisfy all the nanomagnets simultaneously due to the geometry. The current state of the field is to increase the fundamental understanding of ASIs and their complex interactions.

The properties of ASIs are dependent on the temperature of the system. At low temperatures ASIs are stable and can only be changed by an external magnetic field, once the magnetic field is removed the system will remain in the configuration. However, if the temperature increases above a certain threshold the system becomes dynamic with complex interactions. The explicit temperature transition between the two regions are dependent on the dimensions of the nanomagnets and the ASI geometry. Controlling the temperature of the ASIs allows us to determine and adjust if we want the system to be predictable or complex.

Gaining a comprehensive understanding of ASIs requires increased knowledge of the complex interactions in the dynamic region. An important step in this process is to provide platforms which can regulate the temperature of ASIs. This thesis provides the creation and characterisation of an on-chip microheater intended for temperature control of ASIs. The microheater is designed for heat generation and the minimum temperature of the system is therefore restricted by the surroundings and the ASIs needs to be designed accordingly.

Outline

The thesis begins with necessary theoretical background in chapter 3. At first the theory and dynamics of ASIs are explained before the fabrication technique and the most important instruments which have been used are provided. In chapter 4 the design of the microheater, the fabrication steps, thermal characterisation and magnetic contrast analysis are described. After this, the results obtained throughout the thesis are presented and discussed in chapter 5 and chapter 6, respectively. In chapter 7 a conclusion is given and suggestions for future work based on the thesis are discussed.

Chapter 3

Theory

In this section, relevant theory for the thesis is presented. At first, magnetism and ASIs are explained before photolitography is described. After this, important concepts such as ohmic heating, thermal conduction, temperature coefficients and resistance measurements are elaborated. Subsequently, the working principles of important instruments for the thesis are explained. Parts of or whole chapters in section 3.1, section 3.3 and section 3.6.1- 3.6.2 were written as a part of a specialization project involving fabrication of microheaters and are included as the concepts remain relevant.

3.1 Magnetism

Magnetic fields are generated by the movement of electrically charged particles such as electrons, protons, and ions. The magnetic moment of an atom is the vector sum of three contributions which is the spin of the electron, orbital angular momentum of the electron around the nucleus and the change in orbital momentum from a magnetic field [6]. In most cases, these vector sums usually cancel each other and the material exhibits no magnetization.

In *ferromagnetic* materials local magnetic moments align spontaneously. The locally aligned magnetic moments organize themselves into ferromagnetic domains, i.e., areas of the magnetic material where all magnetic moments point in the same direction (Figure 3.1a) [7]. However, when ferromagnetic materials are reduced to nanometer dimensions it is energetically preferred with a uniform magnetization such that all of the magnetic moments align (Figure 3.1b) [7].

(a) **(b)**

Figure 3.1: a) Ferromagnetic material with several domains. b) A single nanomagnet with uniform magnetization.

3.2 Artificial spin ices

ASIs consists of single-domain rectangular nanomagnets arranged in patterns which provides geometrical frustration. The single-domain nanomagnets are bistable and can be characterized by an arrow representing the two possible magnetization states, as seen in Figure 3.2. When nanomagnets are arranged in close proximity to each other, their magnetic fields interact. Each nanomagnet has a preferred magnetization determined by the magnetization of its neighboring nanomagnets. In ASIs, the minimum energy magnetization for each nanomagnet can not be achieved simultaneously due to the geometry of the ASI and the system is therefore considered geometrically frustrated. The ground state is the preferred state of ASIs, providing the lowest energy configuration that the frustrated system can achieve. Two examples of ASIs are given in Figure 3.3 which shows the square ASI (Figure 3.3a) and the 45 ° pinwheel ASI (Figure 3.3b). In ASIs the distance between the nanomagnets are referred to as the pitch and it dictates the magnetic coupling between the nanomagnets.

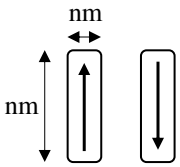

Figure 3.2: The two magnetization states of a bistable nanomagnet.

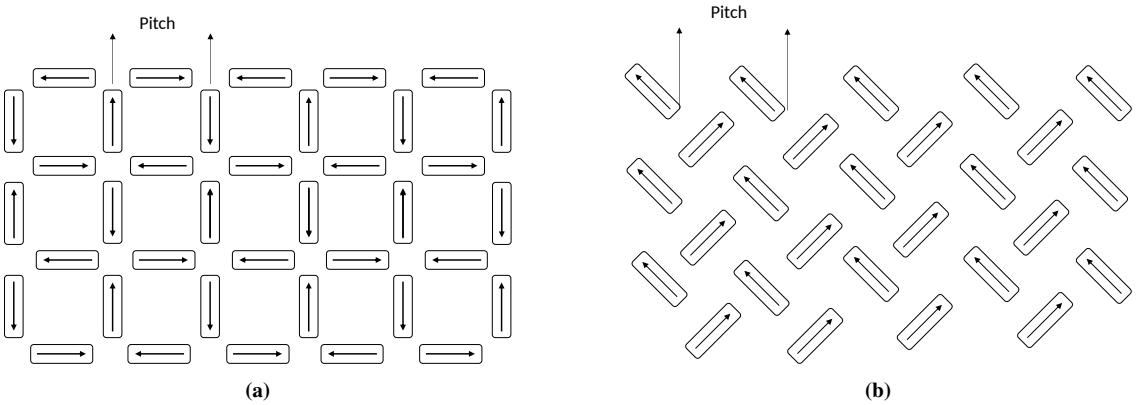

Figure 3.3: Two ASIs consisting of rectangular nanomagnets. a) The square ASIs in the ground state and b) The 45° pinwheel ASI in the ground state.

ASIs are mainly analysed in two temperature regions. The first one is considered the frozen region and the magnetization of the nanomagnets will not change unless an external magnetic field is applied. If an external field is applied, the magnetization of the nanomagnets will change and align to the external field [2]. After the field is removed they will remain in the induced state. If the temperature increases in an ASI system, thermal fluctuations can spontaneously reverse the magnetization of individual nanomagnets and the system is considered to be thermally active. By heating and then cooling down the system, we can manipulate the magnetization. If we gradually reduce the temperature, we achieve the ground state, whereas a rapid reduction may yield interesting alternative states [2]. In this thesis we are interested in the interaction between the nanomagnets when the system is thermally active.

3.3 Photolitography

Photolitography is a technique used for fabrication of integrated circuits and other nanoscale devices [8]. The technique transfers a pattern from a mask to a substrate by the use of UV light. The resolution of the system is primarily determined by the wavelength of the UV light.

At first a patterned mask is placed between the substrate and the UV light. The substrate is coated with a *photoresist*, i.e., a material that changes solubility if it is exposed to light. Photoresist comes in two types, positive and negative. Positive photoresist becomes soluble when it is exposed to light while negative photoresist becomes insoluble. After exposure the soluble parts are removed by submerging the sample in a solvent, which we refer to as a developer. The resist structures obtained by positive and negative photoresist are visualized in Figure 3.4. The photolithography process is visualized in Figure 3.5.

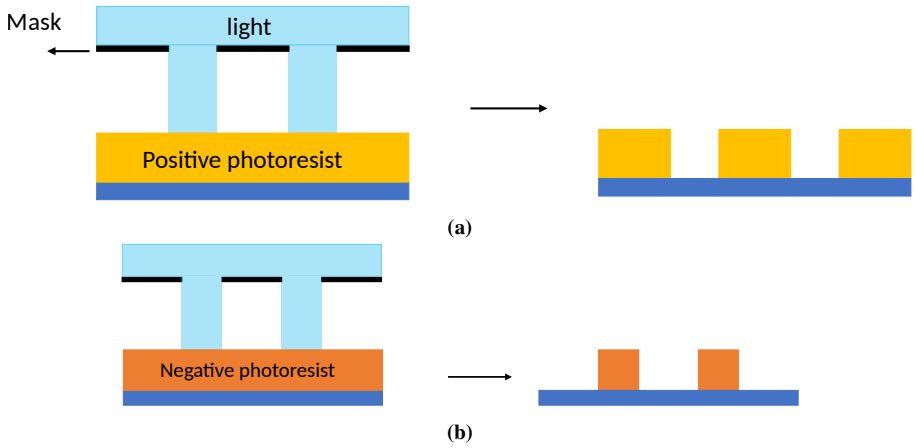

Figure 3.4: The different patterns obtained when using positive and negative photoresist. a) The exposed parts are removed from the final resist structure when using positive photoresist. b) Only exposed parts are present at the final resist structure when using negative photoresist.

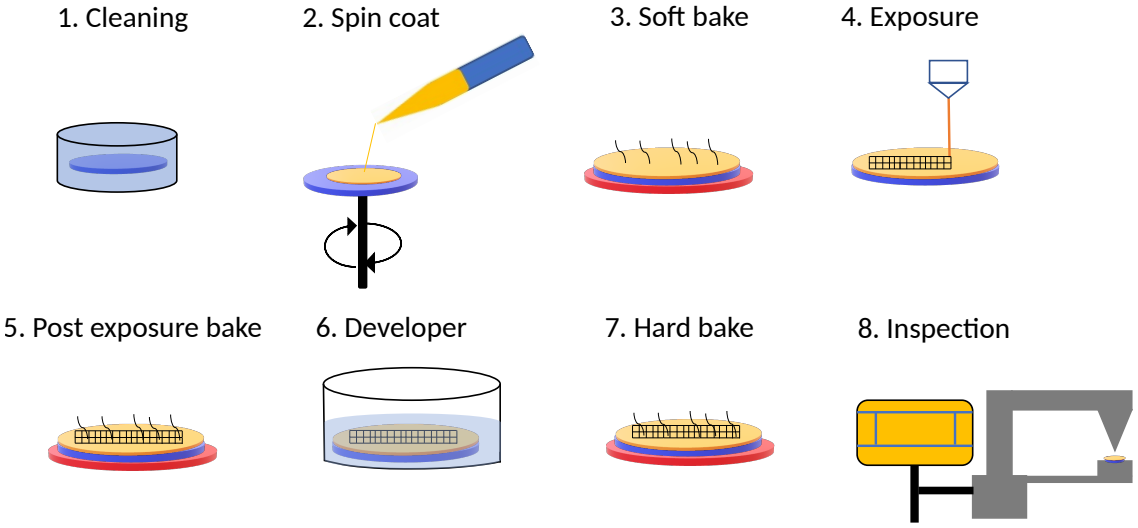

Figure 3.5: The steps involved in a photolitography process. In general the most important steps for understanding the concept is the spin coating (2) to add resist, the exposure (4) to create the pattern and the developer (6) to remove the soluble parts.

1. **Cleaning**
   Cleaning is done to remove particles and unwanted materials on the substrate such that the adhesion between the substrate and resist is optimal. This could be done by cleaning with Acetone and isopropanol or with Plasma and UV ozone cleaning. The type of wafer and available tools decides what process is preferred.

   In some cases it is required with a layer of Hexamethyldisilane (HMDS) on top of the wafer. HMDS is used to increase the adhesion between the photoresist and the wafer. This is not necessary for all resists but can be very useful if poor adhesion is causing problems. The HMDS is deposited by placing the sample and droplets of HMDS inside a confined volume. After this, the air is removed by a vacuum pump and the HMDS evaporates and attaches to the wafer.

2. **Spin coat**
   Spin coating is the most common technique to deposit a uniform resist layer on top of the wafer. The wafer is placed on a rotational holder. After this, resist is dropped at the center of the wafer and the holder begins to rotate. The resist is drawn to the edges with most of it leaving the wafer. The fast rotation ensures a thin and equal layer of resist. Important parameters for spin coating are spin speed/acceleration/time and resist viscosity.

3. **Soft bake**
   After spin coating the photoactive components, i.e., the part of the resist solution that interacts with light, are suspended in a solution. Therefore it is necessary to heat the sample to evaporate the solvent. In addition, the adhesion between the resist and wafer increases.

4. **Exposure**
   Now the sample is prepared and can be exposed such that the desired pattern can be created. This is done by exposing the resist to UV light either by a mask or with a focused lens.

5. **Post exposure bake**
   Some resists need another bake process to amplify or halt the chemical process initiated by the UV light.

6. **Development**
   This step is done to remove the soluble parts by immersing the sample in a suitable solution depending on the type of resist. To stop the process, the sample is transferred to water and nitrogen gas is used to dry the sample.

7. **Hard bake**
   Some resists requires a baking process after development to evaporate unwanted solvent from the developer and improve the adhesion.

8. **Inspection**
   Finally it is necessary to analyze the result and verify that the process went as expected. The final structure is affected by the type of resist, exposure energy and developing time. Typically there are three commonly observed structures during inspection. They are visualized in Figure 3.6. The vertical sidewalls are usually the ideal outcome since the pattern on the substrate will match the mask pattern but this is very hard to achieve. We therefore often need to accept an undercut or overcut resist profile.

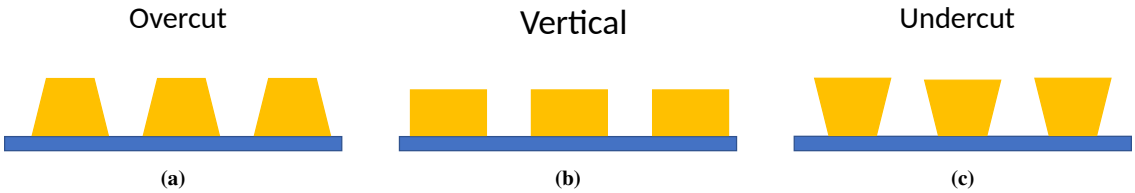

Figure 3.6: Three commonly observed resist profiles in photolitography. a) Overcut profile where the upper parts of the photoresist is more solved than the bottom. b) Vertical wall profile which is the ideal behaviour for transferring the pattern accurately. c) Undercut profile where the bottom parts closer to the wafer is more solved.

3.3.1 Metalization and lift-off

After producing a patterned resist layer on top of the substrate, metalization and lift-off can be done to realize a metal structure of the design. At first a uniform metal layer is deposited across the sample, containing the wafer and the resist structure. Subsequently, the sample is put in a solution where the resist dissolves. In the final structure only the metal layer is present. An illustration of the process is shown in Figure 3.7.

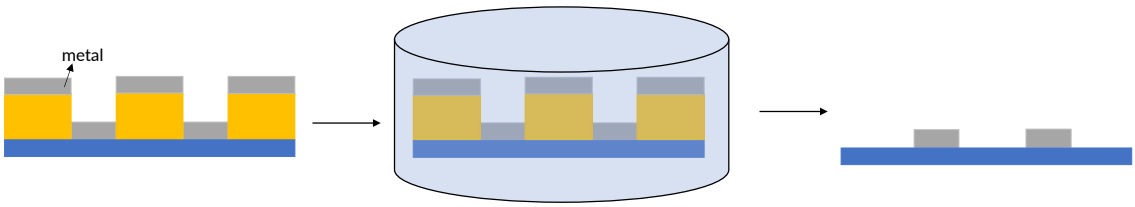

Figure 3.7: At first the wafer is metalized resulting in a uniform metal layer. The resist is then solved, leaving the substrate with a patterned metal layer.

3.3.2 Alignment for multi-layer fabrication

When depositing several layers on a wafer it is necessary to make sure the exposure machine operates with the same coordinate system for both layers. By defining at least two design coordinates on the wafer before the second exposure, the two layers can be aligned. It is common to create equal marks on both layers, making it easy to define the coordinates. In addition it is common to add calipers containing purposely misaligned structures used to measure the misalignment. An example of an alignment mark containing calipers is shown in Figure 3.8.

Figure 3.8: a) Common alignment mark in a multi-layer process. The two layers are represented by different colors. The cross is intended for coordinate reference, and the two calipers are used to measure the horizontal and vertical misalignment. b) Enlarged image of the caliper structures. The misalignment is measured by inspecting which of the branches align since they have a propagating displacement. The numbers are given in nm.

3.4 Ohmic heating and thermal conduction

Ohmic heating occurs when current is passed through an electrical conductor [9]. The thermal energy loss (P) is given by $P = R \cdot I^2$, where R is the resistance of the conductor and I is the current [9].

Metals are often used for ohmic heating since they are good electrical and thermal conductors [10]. When a metal is heated through ohmic heating while being attached to a substrate, a temperature gradient arises. As a consequence, heat is dissipated to the substrate. The pace of the heat dissipation is dependent on the thermal constant of the materials, describing the ability to transfer heat. The thermal conductivity for metals are usually high due to their free electrons [11], copper for instance have $\kappa = 385.0$ W/mK [11]. Semiconductors tend to have lower thermal conductivity e.g., silicon is $\kappa = 167$ W/mK [12]. Gases have the lowest thermal conductivity, e.g., air have κ=26.3 mW/mK [13]. If a metal is used for ohmic heating and attached to a silicon substrate surrounded by air, almost all of the heat generated will be transferred to the silicon until the system reaches a equilibrium [9] because of the low thermal conductivity of air compared to silicon.

3.5 Temperature coefficient and resistance measurements

The temperature coefficient of a material describes the relation between the temperature and the resistance. If the temperature coefficient times the temperature range is low , i.e., ($\alpha\Delta T << 1$), the relationship between the resistance and temperature is approximately linear for metals and mathematically it is written

$$R(T) = R(T_0)(1 + \alpha\Delta T), \tag{3.1}$$

where $R(T)$ is the resistance at a given temperature, $R(T_0)$ is the resistance at the initial temperature and ΔT is the temperature difference($\Delta T = T - T_0$). The temperature coefficient (α) describes the relative change in resistance and the total resistance change is therefore based on $R(T_0)$. Above liquid helium temperatures (4K) the electrical resistivity in metals is dominated by collisions of the conduction electrons with lattice phonons [6]. When the temperature of a metal increase, more phonons are generated which results in more collisions between the charge carriers and the lattice leading to an increased resistance [6].

The resistance of a material is measured by forcing a current (I) through the material and measure the voltage drop (V) [14]. The resistance can be obtained from Ohms law ($V = R{\cdot}I$). Resistance measurements

can be done by two or four point sensing. Two point measurements force current and measure the voltage drop with the same probes, as shown in Figure 3.9a where I_S is the current forced through the conductor and V is the measured voltage drop. The signal through the probes are controlled and measured by a source measure unit (SMU).

Four point measurement uses seperate probes for the current source and the voltage measurement. The advantage compared to two point measurements is that the contact resistance is effectively not included, providing more precise resistance measurements. A current is forced through the material using two probes. To measure the voltage loss, two additional probes are connected to the material in series with a voltmeter. The current through the voltmeter is negligible because of the high impedance in the voltmeter, making the measured voltage independent of the contact resistance. The setup is visualized in Figure 3.9b, I_S is the forced current, V is the measured voltage.

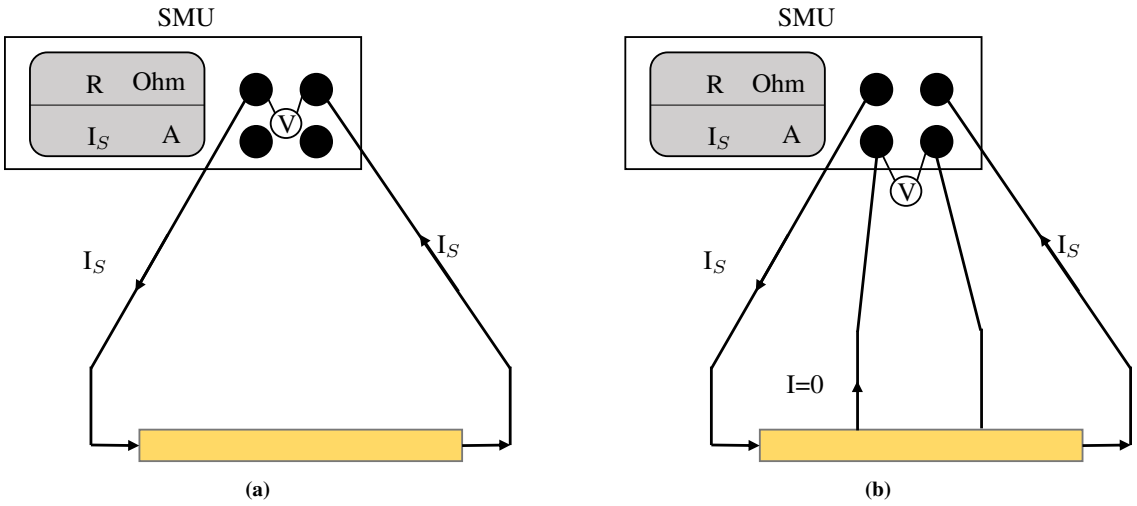

Figure 3.9: The setup for two and four point measurement using a source measure unit (SMU) to control the signals. a) Two point sensing utilizes the same probes to force current and measure the voltage drop. b) Four point measurements utilizes two probes to force a current (I_S) through the conductor and two additional probes to measure the voltage drop (V). The current through the voltmeter is considered to be zero ($I = 0$) and only the material resistance is measured, excluding the contact resistance.

3.6 Instruments

3.6.1 Wire bonding

Wire bonding is a technique used to create connections between electrical contacts. It is done by using a capillary to maneuver a gold wire and applying force, heat and ultrasound energy to form the connections [15]. At first a high voltage is applied to the tip of the metal making the gold wire melt, resulting in a ball at the tip of the capillary. The capillary moves to the first contact pad and initiates contact between the pad and the gold ball (Figure 3.10a). Heat, ultrasound energy and pressure from the capillary deforms the gold ball and makes it adhere to the contact pad. The capillary leads the wire to the second pad and connects them using the same procedure (Figure 3.10b). When the second pad is connected the wire is cut resulting in an electrical connection between the two pads (Figure 3.10c).

The choice of applied force, ultrasound energy, temperature, and contact time depends on the specific material being used. Additionally, the thickness of the pads may vary, further influencing the bonding process. Moreover, the second bonding site, which involves transferring the wire to the second pad, does not initially have a ball shape. Consequently, different parameters may be necessary for these two bond formations [15].

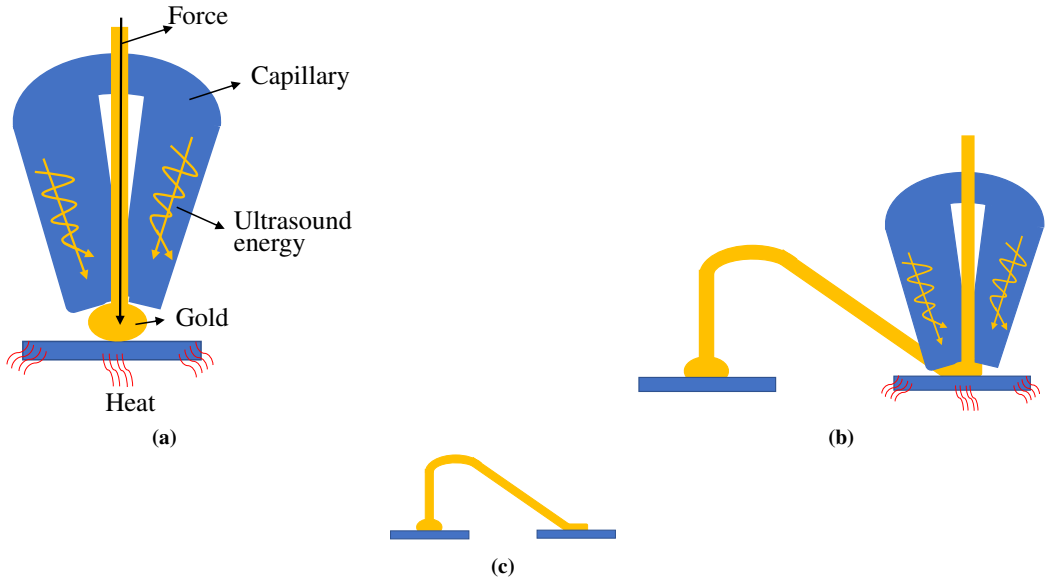

Figure 3.10: The three main steps in wire bonding process. a) The first connection is made by applying heat, force and ultrasound energy. from the capillary to the gold ball. b) Secondly, the wire is lead to the other pad before the same procedure occurs, leaving c) an electrical connection between the two pads.

3.6.2 Electron beam evaporation

Electron beam evaporation is a metalization technique [16] that transfer atoms from a target to a sample by evaporating the target as shown in Figure 3.11. At first free electrons are generated by a current I_C. To move the electrons towards the target it is required with a magnetic field and the electrons need a velocity, due to Lorentz law [16]. An electric field (E) is used to accelerate the electrons towards the magnetic field (B) which bends the electrons towards the target. Electrons will hit the target which eventually evaporates due to the heat generated from the collisions. The evaporated atoms will move towards the sample and attach without colliding with any particles due to the vacuum.

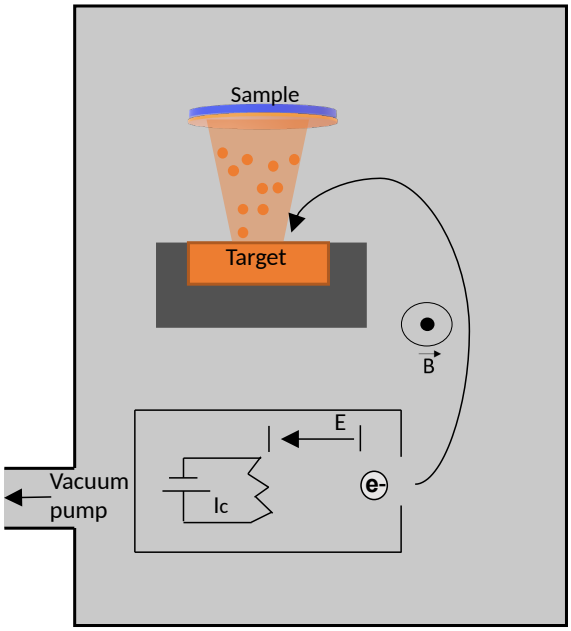

Figure 3.11: Electrons are created, accelerated and bent such that they collide with a target which evaporates, creating a beam of atoms moving towards the sample. The vacuum makes it possible for the evaporated atoms to attach to the sample without colliding with any particles.

3.6.3 Maskless aligner

Maskless aligners are used in the production of microelectronic devices with photolitography [8]. The desired pattern can be accurately transferred onto the substrate by employing a design file. The process involves focusing and modulating light while simultaneously moving the sample, which is positioned on an adjustable stage. The lens adjustments, light modulation and sample movements are optimized from the design file to create the desired pattern. In this thesis, the Heidelberg maskless aligner 150 (MLA 150) [17] was utilized in the fabrication process. The MLA 150 has two wavelength options, $405\,\mathrm{nm}$ or $375\,\mathrm{nm}$ depending on resist which has been spin coated on the sample. The resolution is $1\,\mu\mathrm{m}$ with an alignment accuracy of $500\,\mathrm{nm}$ for multi-layer lithography. The working principle is visualized in Figure 3.12.

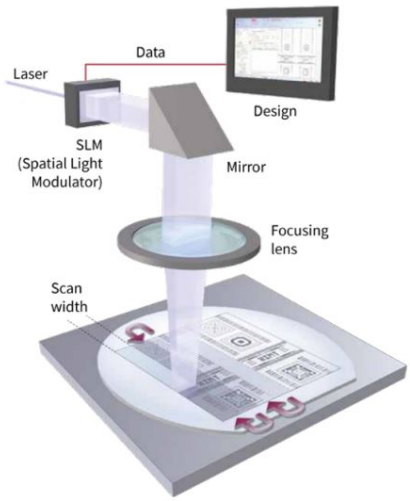

Figure 3.12: Working principle of the MLA150. Image is obtained from [17].

3.6.4 MOKE microscopy

Magneto-optical kerr effect (MOKE) microscopy is an imaging technique used to measure the magnetization of materials. Its working principle relies on the magneto-optical Kerr effect, which rotates the polarization of reflected light depending on the magnetization. In MOKE microscopy, linearly polarized light is directed onto the sample surface, and the reflected light is analyzed for changes in polarization. By measuring the Kerr effect, information about the magnetic ordering can be obtained. This is visualized in Figure 3.13. During MOKE microscopy unwanted information is present, e.g. the topography of the sample, which disturbs the signals of the magnetic ordering. However, these can be removed by taking two pictures with different magnetization and subtracting them [18].

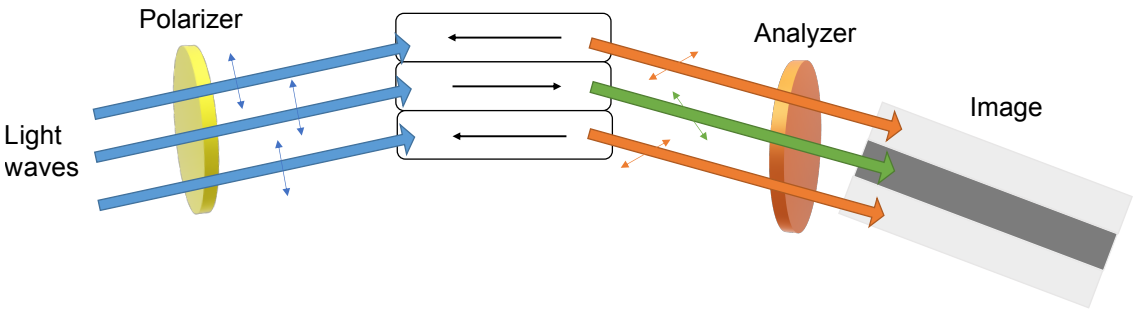

Figure 3.13: The working principle of MOKE microscopy. The magnetization can be analyzed by observing the change in polarization from the incident polarized light.

Chapter 4

Fabrication and experimental

4.1 Microheater Design

The microheater design is inspired by the previous work done by S. Morley et al. [19]. It consists of two components, a heater and a thermometer which surrounds an area intended for ASIs. The heater has two contact pads which are connected through the interdigitated green wires in Figure 4.1 with wire width, W_H, and envelopes the thermometer and the open area for ASIs. Passing current through the heater generates heat via ohmic heating, which then dissipates to the substrate, thereby raising the temperature of the ASIs. The thermometer consists of the purple wires in Figure 4.1 with wire width, W_T, surrounding the open area and consists of four contact pads, making it possible to perform four-point measurements as described in section 3.5. The temperature can be extracted by utilizing the linear relation between the resistance and the temperature in metals. All of the wires have a uniform spacing. The six contact pads are used to connect the microheater to a chip-container with wire bonding and are therefore large compared to the rest of the structure. The design was created in python using the phidl package [20].

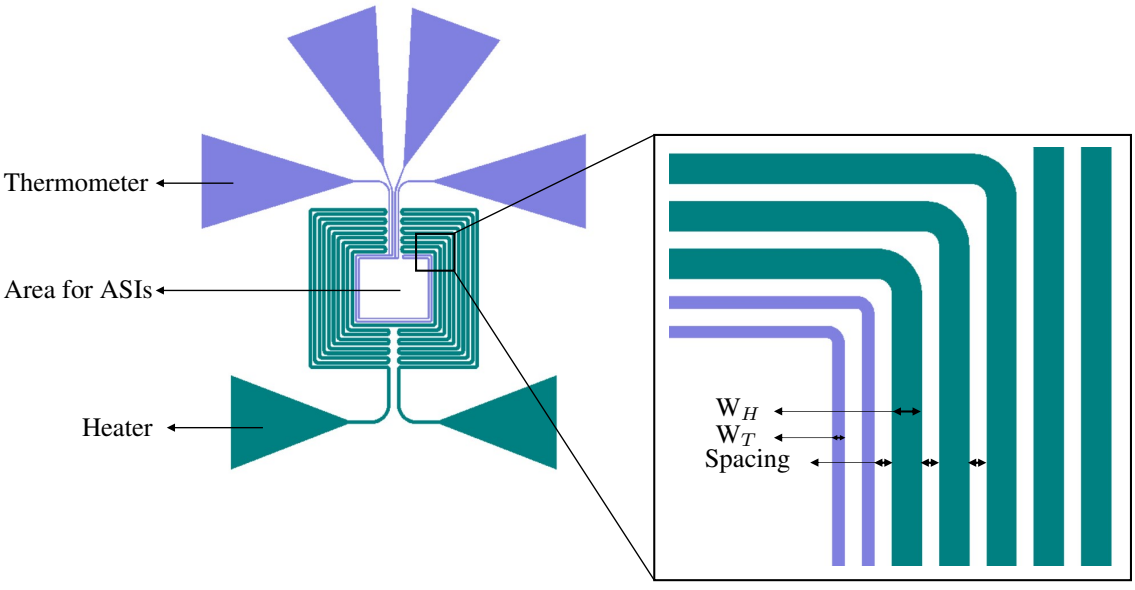

Figure 4.1: The microheater design containing the heater (green) and the thermometer (purple) with an open area intended for ASIs.

Throughout the thesis, the term microheater refers to the total structure, the term heater refers to the heater component and the term thermometer refers to the thermometer component. The design have been altered with minor changes during the thesis but the dimensions and necessary parameters for replication is provided each time it is relevant. When referring to the temperature coefficients of the microheaters it always refers to the temperature coefficient of the thermometer component.

4.2 Fabrication of copper microheaters

As part of a specialization project proceeding this thesis, a gold microheater had previously been fabricated with the parameters $W_H = 24$ µm, $W_T = 10$ µm and 15 µm spacing. The microheater design is given in appendix A. In order to investigate the performance of the microheaters with different metalization, a batch of copper microheaters was fabricated.

The initial fabrication process is given in Figure 4.2 and was identical to the recipe used for the gold microheaters. At first the silicon wafer was rinced with acetone and IPA before dehydration bake for 5 minutes at 150 °C. After this, the wafer was spin coated with SPR700 [21] at a velocity of 4000 rpm/s and 1000 rpm/s^2 acceleration before the sample was soft baked at 100 °C for one minute. The sample was exposed with a dose of 180 mJ/cm^2, followed by a post-exposure bake at 115 °C, and finally developed in MF-26A for 75 seconds.

The fabrication method failed to produce the microheater structures. The exposure dose of 180mJ/cm^2 is relatively high compared to the dose commonly used with SPR700 in nanolab (120-140mJ/cm^2). Therefore a dose test using the same method was attempted but resulted in inadequate microheater patterns. The exposure doses varied from 80-140 mJ/cm^2 with 20mJ/cm^2 per increment.

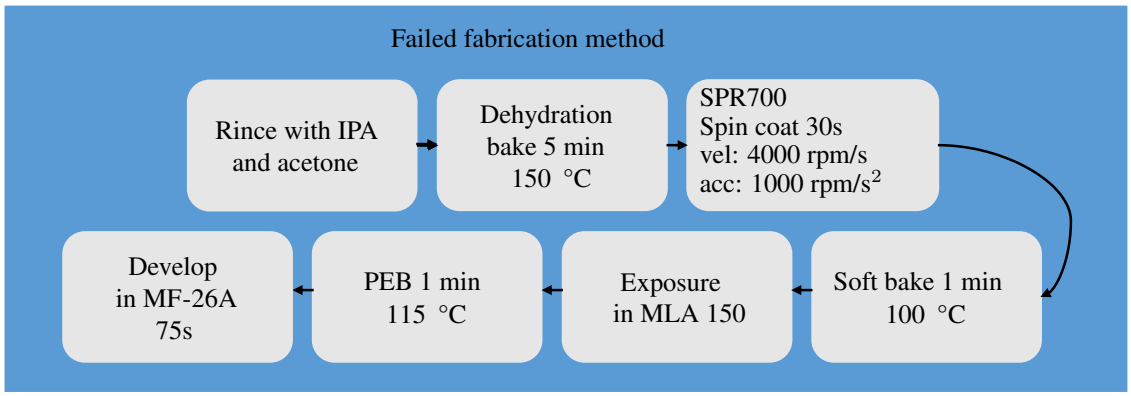

Figure 4.2: Initial fabrication method resulting in inadequate microheater patterns.

All doses failed to transfer the pattern. The inadequate microheater structures were likely caused by poor adhesion. To improve the adhesion, a new dose test was performed but the sample preparation included plasma cleaning [22], before the dehydration bake, to remove contaminants and improve surface wettability. The rest of the fabrication process was unaltered and followed the method given in Figure 4.2. Plasma cleaning was performed for two minutes with 100/100 O_2, i.e., maximum effect with only oxygen gas involved in the process. However, the adhesion did not improve enough to produce the microheater patterns successfully.

In a second attempt to improve the adhesion HMDS was applied for four minutes after cleaning the silicon wafer with acetone and IPA. When using HMDS dehydration bake is not necessary. A new dose test was performed with doses of 80-160 mJ/cm^2 with increments of 20 mJ/cm^2. In this dose test the sample was developed for 40 seconds, the reduced development time was a result of discussion with colleges at nanolab

which developed their samples for a shorter period when working with SPR700 and MF-26A. All of the exposure doses seemed to work as every microheater were successfully developed.

The sample was metalized with a bilayer consisting of titanium and copper, shown in Figure 4.3a, using electron beam evaporation with the configurations given in Table 4.1. The titanium was deposited first to increase the adhesion. After metalization the sample was placed in acetone for 5 minutes for lift-off. Only the microheaters exposed with the dose 140 mJ/cm^2 had complete lift-off for all the structures. The new fabrication method is shown in Figure 4.3b and is the standard fabrication technique throughout the thesis as it can produce the microheater pattern and achieve complete lift-off.

Table 4.1: The configurations during metalization with electron beam evaporation to create copper microheaters.

	Titanium	Copper
Thickness	5 nm	145 nm
Rate	3 Å/s	5 Å/s
Current	120 mA	330 mA
Voltage	10 kV	10kV

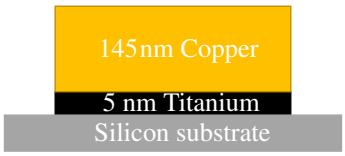

(a)

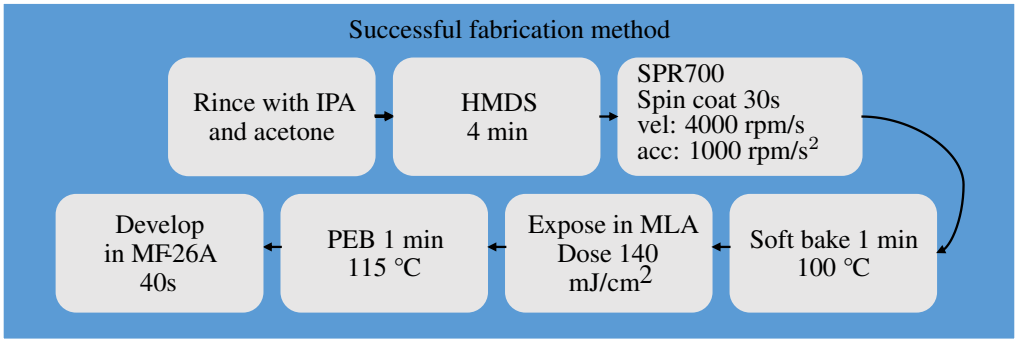

(b)

Figure 4.3: a) Schematic of the metal layer consisting of 5nm titanium and 145 nm of copper. Note that the dimension between the layers are not exact. b) Steps involved in the method to create the microheater pattern successfully and achieve complete lift-off.

4.3 Calibration of temperature coefficients

To determine the temperature coefficients two microheaters, one copper and one gold, were placed on a hotplate at various temperatures. The thermometer resistance was measured at each temperature. Two adjustable probes connected to a SMU were placed on thermometer pads and performed two point measurements of the resistance. It is assumed that the heat generated from the thermometer resistance measurement is negligible. The setup is visualized in Figure 4.4, where the I_C is the current forced through the microheater and was 1 mA during the measurements for both microheaters.

Eight measurements were done within the temperature range of 30-130 °C for the gold microheater and six measurements were done between 25-130 °C for the copper microheaters. The average resistance and standard deviation was found over a period of 1 minute at each temperature.

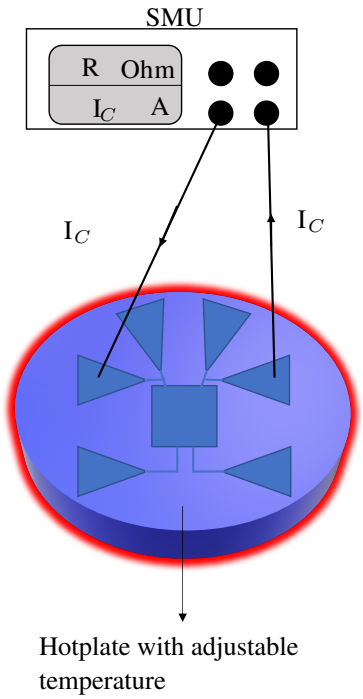

Figure 4.4: Calibration of the temperature coefficients for the microheaters. The microheaters were placed on a hotplate and probes were used to measure the thermometer resistance at various temperatures. The heater structure is not to scale but the pads which were used are correctly illustrated.

4.4 Fabrication of microheaters with ASIs

The ASIs and the microheaters are fabricated with different techniques. The behaviour of the ASIs are more sensitive to contaminations on silicon wafer due to the nanometer dimensions of the structures. Therefore the ASIs are deposited first and subsequently the microheaters.

The nanomagnets were fabricated by Ida Breivik from the research group. The fabrication was done with electron beam lithography using a 1:2, CSAR62:anisole electron beam resist and AR600-546 developer. Permalloy and aluminum (Al) were deposited with the configurations summarized in Table 4.2. The permalloy is the magnetic material used to create the nanomagnets and the Al layer protects against oxidation. The square ASI and 45° pinwheel ASI, were deposited with varying pitch. The design is provided in appendix B and 16 ASI structures were fabricated on the silicon wafer.

Table 4.2: Electron beam evaporation metalization for nanomagnet deposition.

	Permalloy	Al
Thickness	10 nm	2 nm
Rate	2 Å/s	1 Å/s
Current	36 mA	110 mA
Voltage	8 kV	8 kV

After creating the ASIs, the microheaters were fabricated using the method given in Figure 4.3b. The design had wire widths, $W_H = 25$ µm, $W_T = 10$ µm and a wire spacing of 15 µm. In addition, alignment marks were added to the design which is given in appendix C. Before metalization, the wafer was scribed into two pieces, each containing eight microheaters. Both pieces were metalized with titanium (5nm) and gold (145 nm) using the configurations given in Table 4.3. The first batch was metalized a couple of days after the resist pattern was fabricated and the second batch was metalized two weeks later. The choice of gold metalization increases the chance of successful wire bonding as gold adhere more easily to gold than copper [15]. After metalization it was performed lift-off using acetone for 5 minutes.

Table 4.3: The configurations during metalization with electron beam evaporation to create gold microheaters.

	Titanium	Gold
Thickness	5 nm	145 nm
Rate	3 Å/s	5 Å/s
Current	120 mA	330 mA
Voltage	10 kV	10kV

4.5 Test chamber for thermal characterisation

To control the heater current and perform 4 point measurements simultaneously, a custom test chamber was required. The test chamber was design and created by elprolabb at NTNU. The system consists of six coaxial connections, labeled 1-6 in Figure 4.5a. Each connection has a reference ground signal (VSS) and an output signal from the SMU. The setup makes it possible to connect two SMUs to the system, as seen in Figure 4.5b. The colored wires in Figure 4.5a are attached the test chamber. The chip-container must be attached to the test chamber to connect the microheater to the coaxial signals. The process for connecting the microheater to the experimental setup is given in Figure 4.5c. The finalized system of the test chamber are given in appendix E.

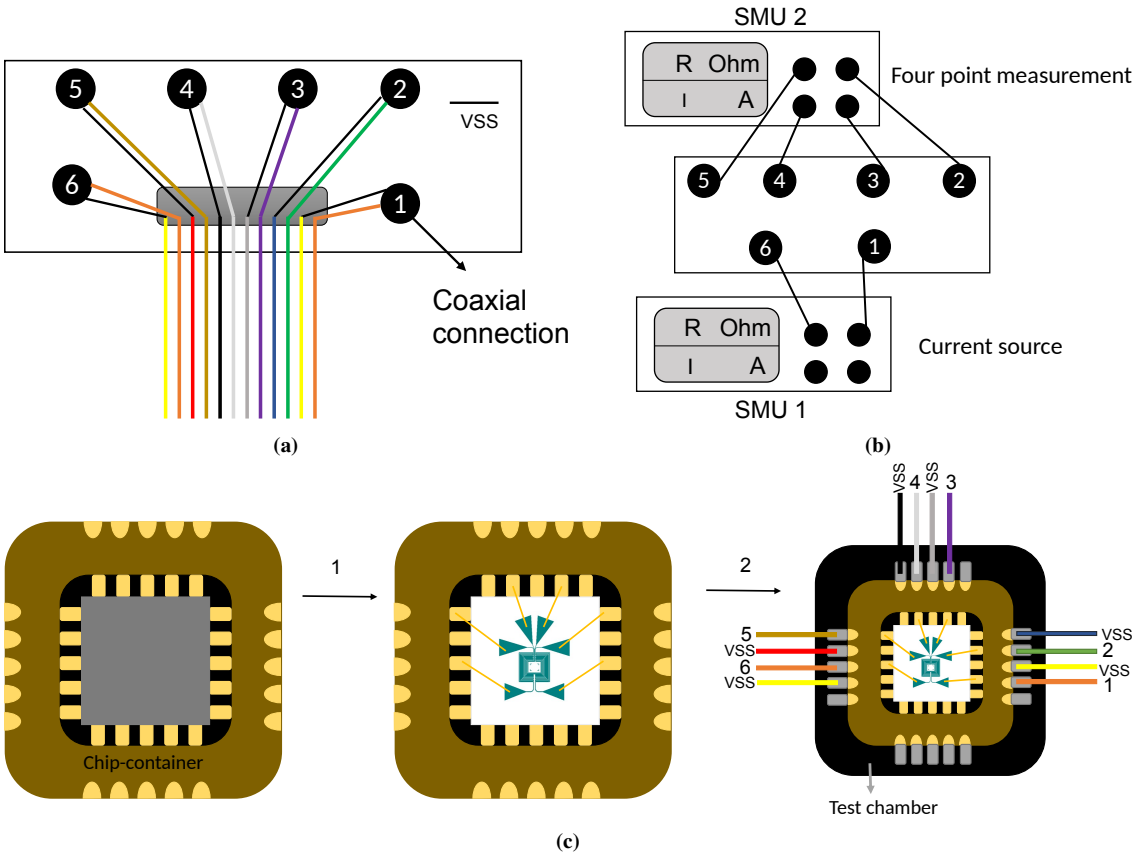

Figure 4.5: a) Six coaxial connections with reference signal and input signals which can be connected to b) two seperate SMUs used for current control and resistance measurements. c) The steps required to connect the microheater to the test chamber.

4.6 Wire bonding and current sweeps

Initially, a gold microheater without ASIs was wire bonded to the chip-container with the parameters listed in Table 4.4. The chip-container was attached to the test chamber. Two additional probes were required to perform the experiment due to errors with the PCB. One probe was placed on one heater pad and the second probe on a thermometer pad. The current through the heater was then swept from 1mA-1A. The motivation behind the current sweep was to observe the increase in resistance as the heater current increased.

Table 4.4: Parameters used for wire bonding.

Parameters	Bond 1	Bond 2
Ultrasound energy [W]	200	250
Time [ms]	200	200
Force [gF]	25	35
Temperature [°C]	100	100

.

To perform a second sweep, a new microheater with ASIs was successfully connected to the chip-container by wire bonding. All of the pads were connected to the chip-container with the parameters listed in Table 4.4. Two of the pins connecting the test chamber to the chip-container were not in contact and it was therefore not possible to perform four point measurements. However, it was still possible to measure

the resistance through the thermometer with standard two point measurements. The experiment involved varying the heater current between [0,40] mA with step responses and measure the transient response of the thermometer resistance.

4.7 MOKE experiment

The initial experiment employing MOKE microscopy aimed to initialize the ASIs and observe changes in the magnetization when the temperature was increased by the heater. It was not possible to achieve sufficient focus in the microscope because the test chamber prohibited the microscope to get close enough to the sample. The test chamber was removed to reduce the height and by using conducting sliver glue the heater pads were connected directly to the wires for coaxial 1 and 2, which is illustrated in Figure 4.7. The microheater was placed back into the MOKE microscope for another attempt at the magnetization of the ASIs.

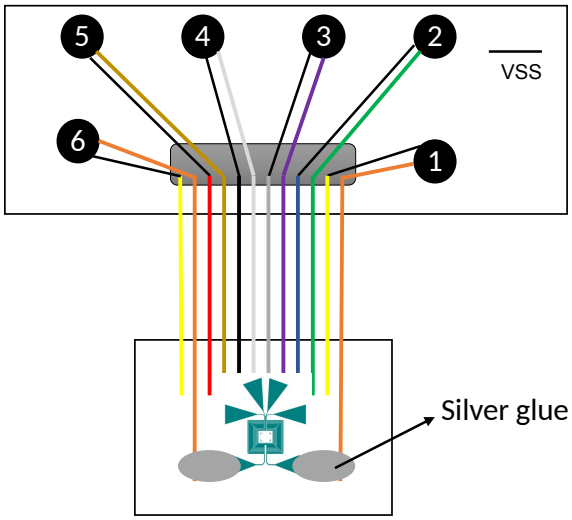

Figure 4.7: Conducting silver glue connects the microheater to coaxial 1 and 2 such that the heater current can be controlled.

Chapter 5

Results

In this chapter the results obtained throughout the thesis will be presented. Firstly, the results from the fabrication process of the copper microheaters are presented. Secondly, the temperature coefficients obtained from calibration of gold and copper microheaters are given. After this, the fabrication process of the microheaters with ASIs are presented. Subsequently, the wire bonding results and measurements from the thermal characterisations are presented. Finally, the results obtained from MOKE microscopy are given.

5.1 Fabrication of copper microheaters

The fabrication of copper microheaters required three different batches of fabrication to successfully produce the microheater resist pattern. All of the batches were analyzed by optical microscopy and the results are summarized in Figure 5.1. The bright parts are wafer and the darker parts are resist. The initial fabrication method (Figure 4.2) failed to produce the microheater pattern, as shown seen in Figure 5.1a. The resist lines did not adhere to the substrate. The second attempt involving plasma cleaning provided similar results with detached resist lines and inadequate microheater patterns. Applying HMDS solved the problem and the microheater pattern was transferred successfully, as shown in Figure 5.1b.

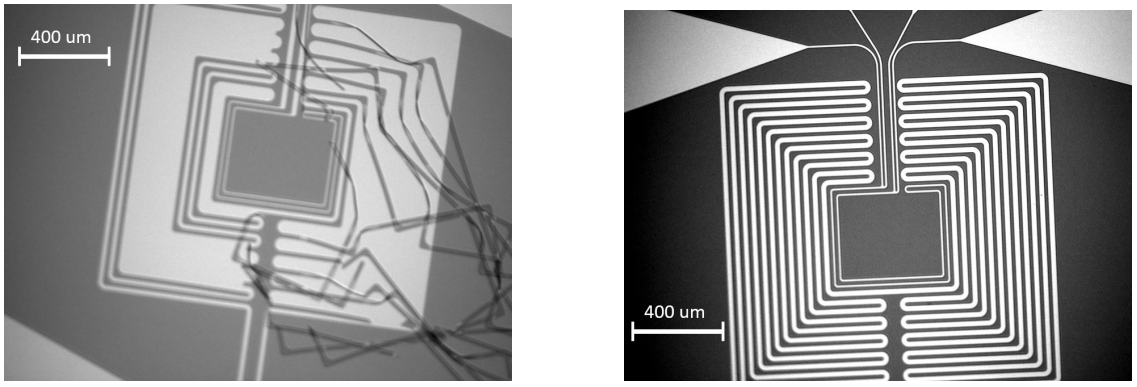

(a) **(b)**

Figure 5.1: a) The result from the initial fabrication recipe. b) The result from the adjusted fabrication method including HMDS before spin coating.

After metalization and performing lift-off, the microheaters were analyzed by optical microscopy. All of the exposure doses between 80 mJ/cm^2 to 160 mJ/cm^2, except for 140 mJ/cm^2, experienced incomplete lift-off with residual metal being present between wires, as shown in Figure 5.2a. In Figure 5.2a, residual metal is also present in the area intended for ASIs.

The microheaters with an exposure dose of 140mJ/cm^2 resulted in complete lift-off (Figure 5.2b) for all four microheaters as the metal in-between the wires and inside of the ASIs sample area were properly removed.

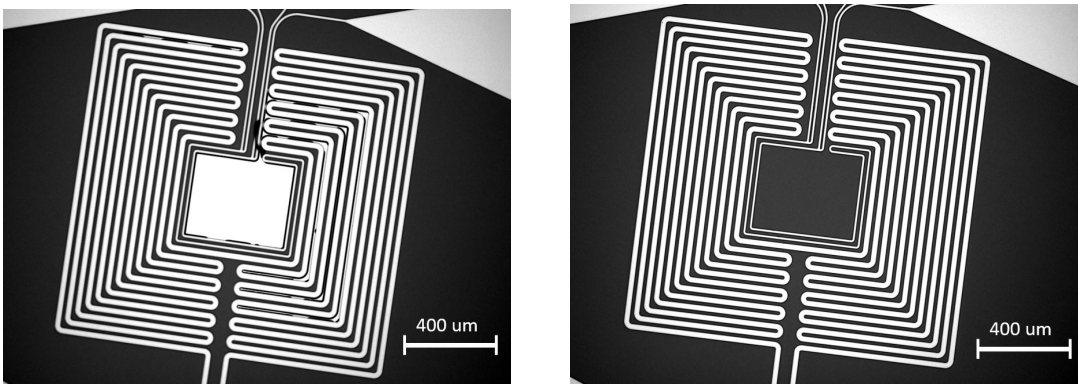

(a) **(b)**

Figure 5.2: An example of a) incomplete lift-off for a microheater exposed with 80 mJ/cm^2 and b) complete lift-off for a microheater exposed with 140 mJ/cm^2.

5.2 Calibration of temperature coefficients

After fabrication of the microheaters, the temperature coefficients were measured using the method described in section 4.3.

The relation between the temperature and the thermometer resistance for both microheaters are shown in Figure 5.3. The blue and red dots are measured data points used to create the regression lines. The data shows a linear relation between the resistance and the temperature for both metals. The gold thermometer has a lower resistance and temperature coefficient, as indicated by the data points and the slope of the regression line. The calculated temperature coefficients and standard deviations of the linear regressions are given in Table 5.1. The average and standard deviation for each data point in Figure 5.3 are given in appendix D.

Table 5.1: Estimated temperature coefficients and standard deviation for the regression lines.

	Estimated $\alpha[\Omega/\mathrm{C}^\circ]$	Standard deviation of regression line $[\Omega/\mathrm{C}^\circ]$
Copper	$2.98 \cdot 10^{-3}$	0.32
Gold	$2.51 \cdot 10^{-3}$	0.34

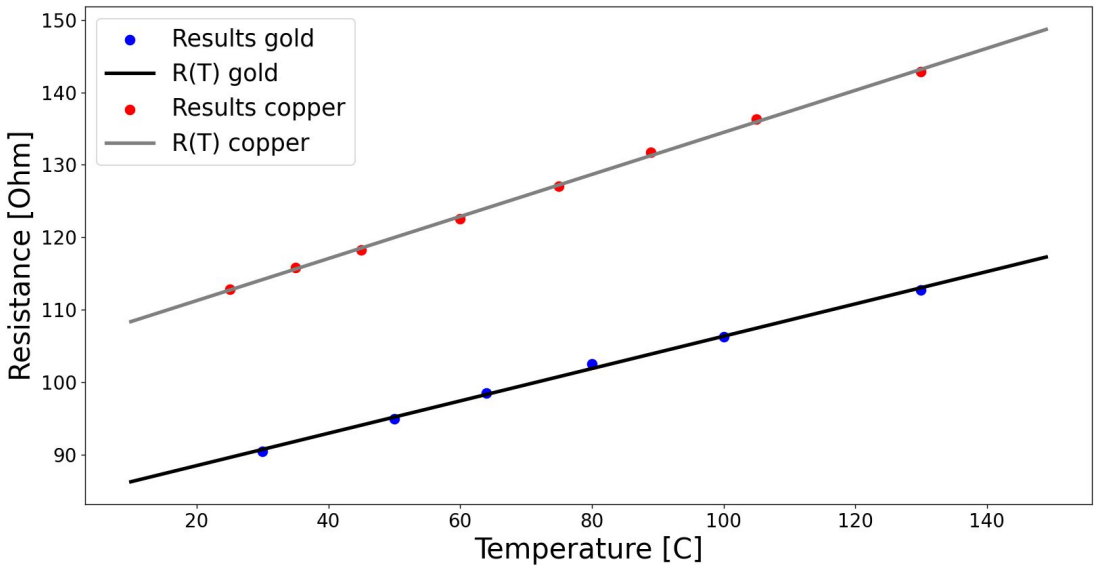

Figure 5.3: The thermometer resistance as a function of temperature for a gold and copper microheater.

5.3 Fabrication of microheaters with ASIs

The ASIs were fabricated prior to the microheaters. In preparation for the second exposure, alignment marks were defined to ensure that the coordinate systems remained consistent for both exposures.

After development, the sample was analyzed by optical microscopy. The microheater layer had a significant alignment error relative to the ASIs layer. The alignment marks used in the second exposure are shown in Figure 5.4 and the displacement were manually measured. The misalignment for each corner is summarized in Table 5.2. Corner A is well aligned but corner B has a major displacement in the vertical direction, corner C has a major displacement in the horizontal direction and corner D has a major displacement in both directions. If the layers were aligned it would be expected to see four corners with similar alignment as corner A in Figure 5.4.

Table 5.2: Vertical and horizontal displacement of the four alignment marks.

	Horisontal displacement [µm]	Vertical displacement [µm]
A	~ 0	0.27
B	~ 0	5.61
C	5.25	0.27
D	5.66	5.92

Despite the alignment error, all of the ASIs were inside of sample area and was surrounded by the microheater structure. In addition, the microheater patterns were clearly distinguishable from the resist as seen in Figure 5.5. Some internal alignment marks, seen as red structures in Figure 5.5, were deposited on top of ASIs at the edges. However, undamaged ASIs were present for all microheater, making it possible to analyze the magnetic contrast in the sample.

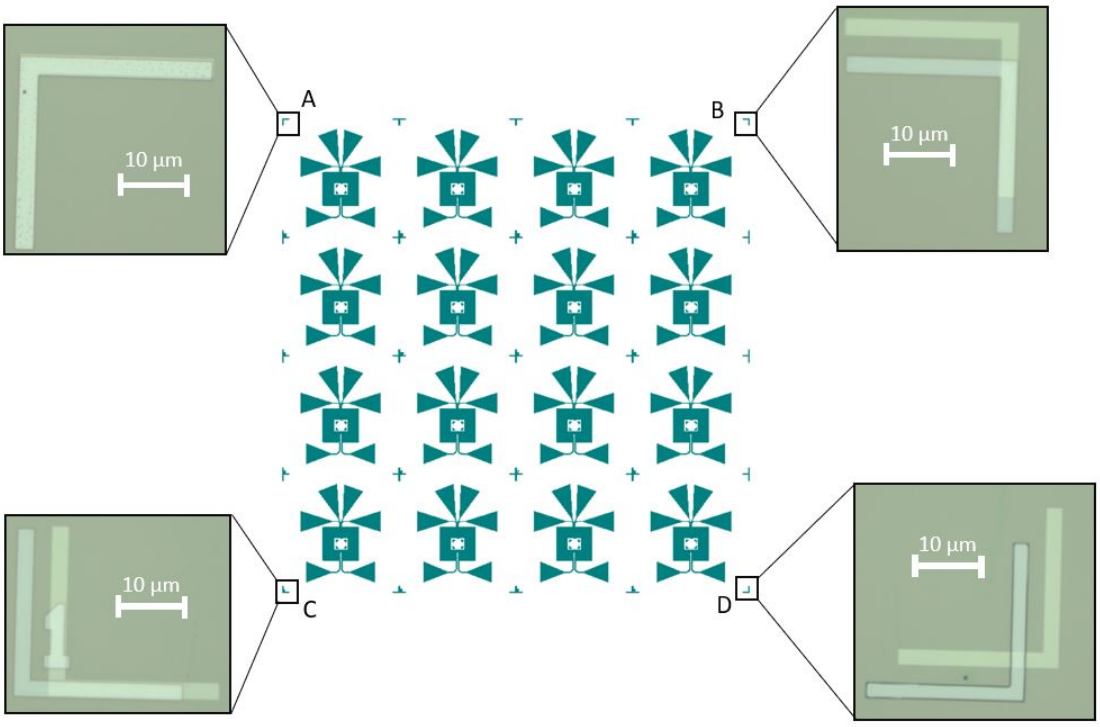

Figure 5.4: The alignment marked defined in the second exposure with enlarged images showing the alignment of the four corners.

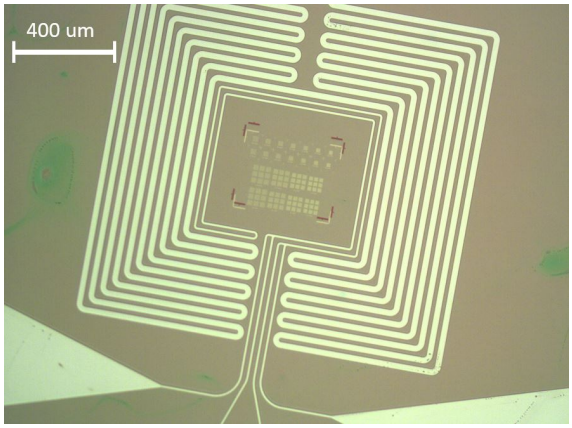

Figure 5.5: Microheater resist structure with ASIs inside of the sample area.

Optical microscopy of a single microheater after development is provided in Figure 5.6 and has wider wire widths than the design. The designed wire widths for the heater and thermometer were $W_H = 25$ µm, $W_T = 10$ µm and 15 µm spacing. The measured widths where $W_H = 25.4$ µm, $W_T = 11.0$ µm and 14.5 µm spacing. The three visible heater wire widths were measured with consistent results. The wire spacing was also measured multiple times with consistent results. Initially, the measurements were obtained by an intrinsic tool in the optical microscopy software but these were deemed inaccurate, shown as red lines in Figure 5.6. The provided measurements were therefore obtained my placing lines manually and compare them to the reference line of 20 µm.

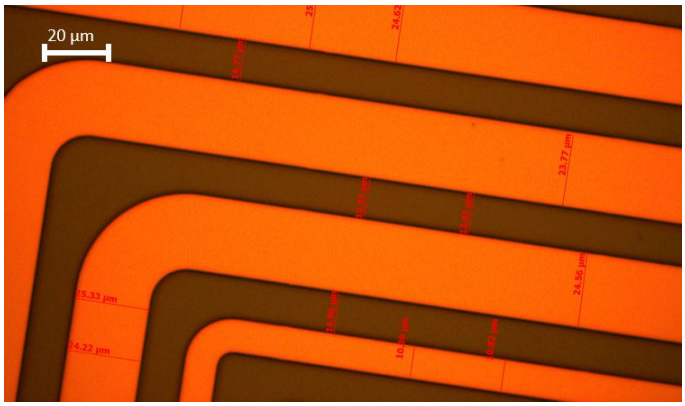

Figure 5.6: Optical microscopy of a microheater resist structure with ASIs. The image was used for wire widths and spacing measurements.

After metalization and performing lift-off, the microheaters containing ASIs were inspected by optical microscopy. Nine of sixteen microheaters looked acceptable. One of the structures with complete lift-off is shown in Figure 5.7a. There are no residual gold present and the wires are not damaged. Four microheaters had incomplete lift-off with residual gold being present between the wires, as shown in Figure 5.7b. The residual gold is attached between the heater and thermometer wires. In addition, the space between the heater wires are filled with gold, as can be seen in the top region in of Figure 5.7b. Parts of the inner thermometer wire is also missing in Figure 5.7b.

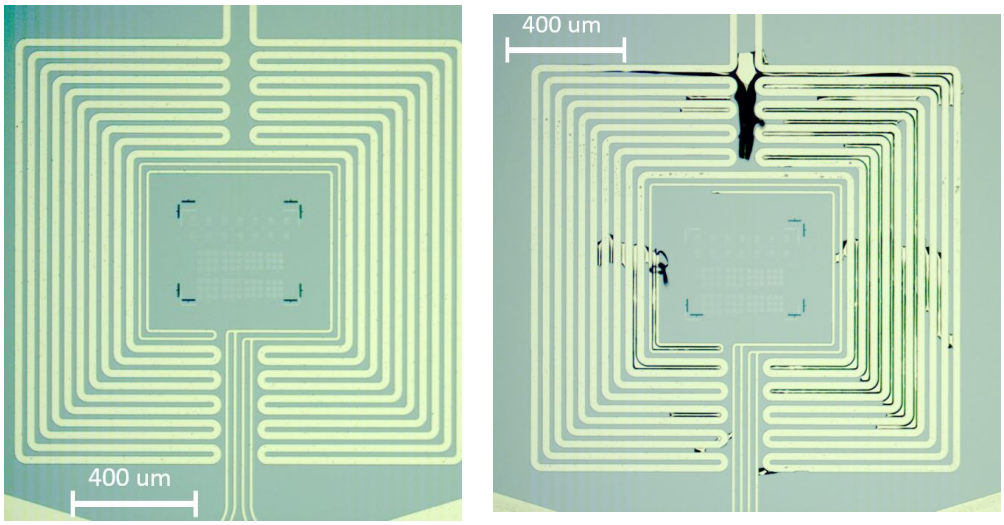

(a) **(b)**

Figure 5.7: a) One of the microheaters with complete lift-off and b) one of the microheaters with incomplete lift-off.

Three microheaters had detached heater wires, as shown in Figure 5.8, indicating poor adhesion between the Ti/Au stack and the silicon wafer.

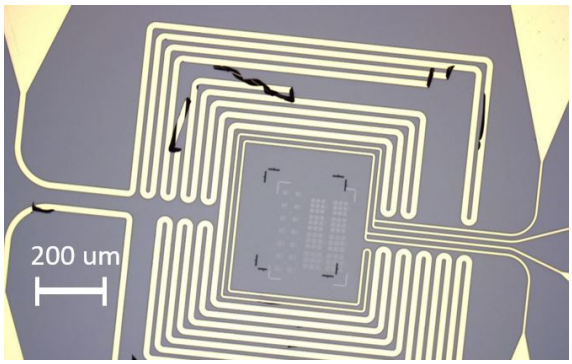

Figure 5.8: Detached wires during lift-off resulting in inadequate microheaters.

5.4 Wire bonding of microheaters to chip-container

Wire bonding was conducted a total of three times and analyzed by optical microscopy. The first wire bonding was performed on a gold microheater without ASIs and was successful, as shown in Figure 5.9. The wire bonding seemed to establish an electrical connection from the microheater contact pads (Figure 5.9a) to the chip-container (Figure 5.9b). Note that the chip-container is reused and has been connected to other devices through wire bonding which can be seen by the residual gold circles at the connection pads in Figure 5.9b. All of the microheater contact pads were connected to the chip-container.

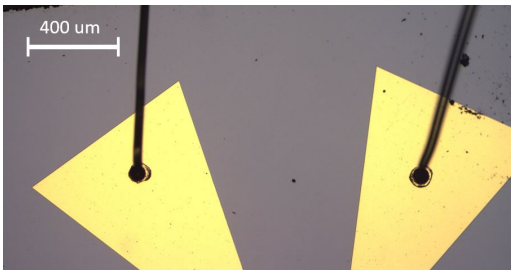

(a)

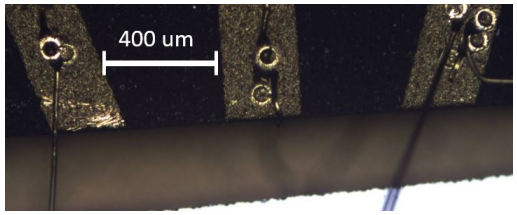

(b)

Figure 5.9: a) The wire bonding results from the two upper thermometer contact pad with their resulting b) wire bonds at the chip-container.

The second and third wire bonding involved two gold microheaters with ASIs. They required many attempts to form connections at the microheater contact pads as shown in Figure 5.10. Each circle on the contact pad represents a wire bonding attempt where the gold ball formed a connection and then detached, leaving behind a hole. These holes are indicated by circles of the same grey color as the background . The second attempt resulted in two wire bonds to the chip-container, one for each heater pad. The third attempt resulted in all pads being connected to the chip-container.

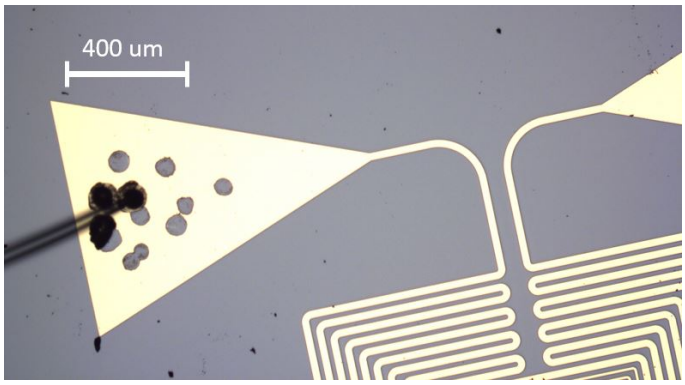

Figure 5.10: Wire bonding process which required many attempts to form a connection at the pad. Each hole in the contact pad represents one wire bonding attempt.

5.5 Current sweep and MOKE microscopy

Thermal characterisation was enabled by attaching the chip-container to the test chamber and control the signals and measurements by using two SMUs.

The first current sweep through the heater from 1mA to 1A resulted in a burned microheater as seen in Figure 5.11. The color of the wires is much darker on certain parts of the heater indicating oxidation or some chemical reaction. In addition, the pads in Figure 5.11b looks damaged as the color near the wire is black compared to the edge of the pad which is brighter. Contaminations on the heater is evident from the black area observed on the heater wires in Figure 5.11a. In addition, the wires are damaged, as can be seen by the diagonal lines across the microheater in Figure 5.11a.

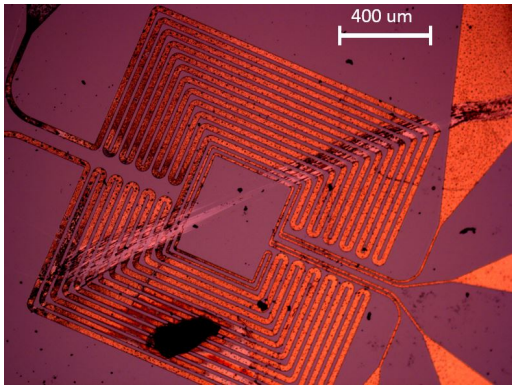

(a)

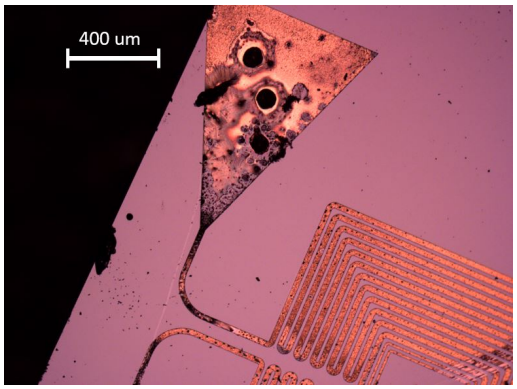

(b)

Figure 5.11: Microheater used for the initial current sweep, resulting in a) a burned microheater with b) a burned heater pad.

The second current sweep through the heater was used to measure the resistance in the thermometer as the temperature was regulated by the current through the heater. The resistance and current measurements for both the thermometer and the heater are shown in Figure 5.12. Since the results were obtained from two seperate SMUs, the time axis of the two plots, are not aligned as there is an offset present. However, the sudden changes in resistance can clearly be matched to the different current levels. The data was further analyzed by a 5th order Butterworth low pass filter to visualize the trend and filter out noise [23].

The transient response of the thermometer resistance seems to be an exponential or asymptotic function as it increases rapidly in the beginning before it takes time to stabilize. The resistance stabilizes in all regions

except for region 3 and 7, where the resistance continues to increase. It took approximately 30 seconds for the blue transient in Figure 5.12a to reach 80% of the level difference between region 1 and 0. It took the transient in region 2 approximately 48 seconds to reach 80% of the level difference between region 2 and 1. When regulating the temperature down, the opposite characteristics can be seen in region 4, 5 and 6. It takes 23 seconds to reach 80 % of the resistance decrease in region 3 and 55 seconds to reach 80% of the resistance decrease in region 5.

The stabilized resistance in region 4 is a bit higher than the stabilized resistance in region 2 even though the heater current is the same for the two regions. The discrepancy is also seen for the region pairs 5/1 and 6/0. It can also be seen that the first current shift to 10 mA in region zero corresponds to a negligible shift in the thermometer resistance.

The increments in the step functions were 10 mA between the regions 1, 2 and 3, as seen in Figure 5.12b. The difference between the stabilized values in region 2 and region 1 is significantly smaller than the difference between the final values in region 3 and the stabilized value in region 2. The relation shows that constant increments in current does not result in a constant increase in the thermometer resistance.

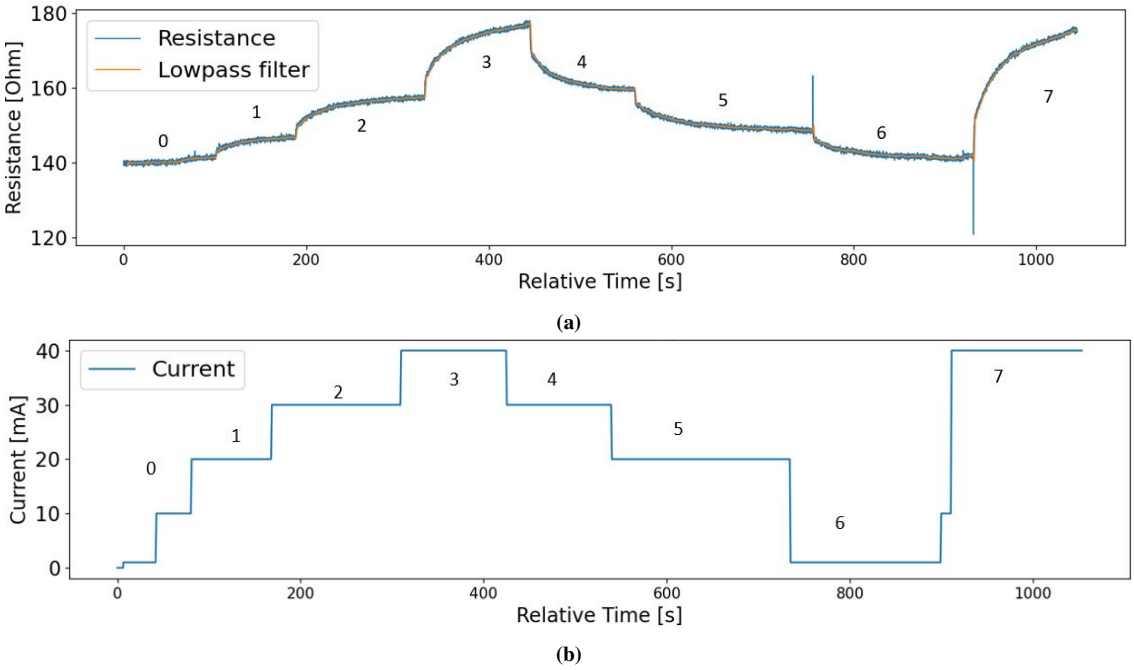

Figure 5.12: a) The measured resistance of the thermometer and b) the current through the heater. Note that the time axis are different since the data was obtained from two seperate SMUs.

The test chamber could not achieve sufficient focus during MOKE microscopy and was removed to increase the focus. However, the magnetic contrast was not strong enough and it was not possible to observe the magnetic contrast in the ASIs.

Chapter 6

Discussion

In this chapter the results obtained from the fabrication processes, thermal characterisation and MOKE microscopy will discussed. The order will be the same as they were presented in chapter 5 beginning with the fabrication of copper microheaters and calibration of the temperature coefficients. After this, the fabrication results from microheaters containing ASIs are discussed before wire bonding and findings from the thermal characterisation are elaborated. Finally, the attempted MOKE microscopy is discussed.

6.1 Fabrication of copper microheaters

The initial fabrication technique, shown in Figure 4.2, failed to produce the microheater pattern. The presence of detached lines in the resist structure (Figure 5.1a), representing the heater wires, are caused by poor adhesion between the silicon wafer and the resist. At first, plasma cleaning was performed in an attempt to increase the adhesion but it failed. Plasma cleaning only makes the surface cleaner but does not enhance the adhesion with chemical interactions [22]. The removed contaminations were not enough to increase the adhesion and the microheater structures were inadequate. In a second attempt to improve the HMDS was employed, resulting in successful microheater structures, as shown in Figure 5.1b. Based on these findings, it is fair to conclude that inconsistent adhesion between the silicon wafer and the resist was the problem for the inadequate microheater structures.

The initial fabrication method (Figure 4.2) successfully produced the gold microheater used in the calibration of the temperature coefficients. The method did not include HMDS and both fabrication procedures were done in the same laboratory using the same equipment. The SPR700 resist had been switched since it was used in the previous method for the gold microheater. Therefore changes in chemical properties of the resist such as sensitivity or chemical bonds could affect the adhesion or require adjustments in spin coating, the exposure dose or developing time. In the attempt to adjust these parameters only the exposure dose was varied. The development remained constant at 75 seconds before it was changed to 40 seconds in the same process as HMDS was included. The initial long developing time of 75 seconds could have contributed to poor adhesion. Over development could cause adhesion problems since it will remove more resist than intended, leaving a smaller contact area between the resist and the wafer. The reduced contact area will be more sensitive to contact with the developer and solid resist might detach from the wafer due to the decreased adhesion [8]. Since it was adjusted in the same process which included HMDS we do not know if over development caused adhesion problems.

After metalization and performing lift-off the copper microheaters fabricated with several exposure doses were analyzed by optical microscopy. The microheaters which were exposed with a dose of 140 mJ/cm^2 had complete lift-off, as shown in Figure 5.2b. All of the other exposure doses had at least one microheater

with incomplete lift-off, as shown in Figure 5.2a. It might be a coincidence as it was only fabricated four microheater with each dose. However, since one dose achieved complete lift-off for all microheaters it was decided to use this in the future fabrication recipes. The optical microscopy images in Figure 5.2 are taken after leaving the sample in acetone for 5 minutes. When incomplete lift-off was discovered, the sample was placed back into the beaker of acetone for a few minutes, before it was thoroughly showered with acetone in an attempt to remove the residual gold. The attempt failed and residual gold was still present for most of the microheaters. The incomplete lift-off could occure from metal being attached to the sidewalls which makes it difficult to remove. Another explanation for the incomplete lift-off could be the resist height relative to the metal height. If the margin is too low it could cause problems during lift-off as the acetone will struggle to dissolve the resist. The resist layers were measured between 940-980 nm throughout the process and 150 nm of metal were deposited. To investigate this further the parameters during spin off can be altered to create a thicker resist layer which can metalized and inspected after lift-off.

6.2 Calibration of microheaters

The microheaters were placed on a hotplate at several temperatures while the average thermometer resistance was measured over a period of one minute. The thermometer resistance increased linearly with the temperature, as shown in Figure 5.3 and demonstrated the intended core functionality of the thermometer. The temperature coefficients were estimated to be $2.51\,\mathrm{m\Omega/C^\circ}$ for gold and $2.98\,\mathrm{m\Omega/C^\circ}$ for copper which is lower than the bulk temperature coefficient for both materials ($3.72\,\mathrm{m\Omega/C^\circ}$ for gold and $4.041\,\mathrm{m\Omega/C^\circ}$ for copper [14]). Thin films are expected to have a smaller temperature coefficient than bulk materials due to their reduced size, making the resistance less dependent on the temperature of the material [24]. It should be noted that the temperature coefficients are consistent as $\alpha_{Au} < \alpha_{Cu}$.

The most important characteristic is the linear relation between the resistance and temperature. It does not affect the intended use that the temperature coefficients are lower than the bulk values. However, it is of interest to measure the temperature coefficient of several gold and copper microheaters for comparison. If the estimated coefficients align for several microheaters with equal metalization it would be possible to obtain the temperature and resistance characteristics by measuring the thermometer resistance at room temperature such that the relation can be obtained from eq. (3.1). It is reasonable to assume that this should be the case since temperature coefficients of thin films are very dependent on the metalization process and the microheaters were metalized with the same instrument using identical configurations [24]. However, if the settings were to be changed in future fabrication processes it would be necessary with a new calibration.

6.3 Fabrication of microheaters with ASIs

The microheaters were fabricate such that the initially deposited ASIs were inside of the sample area (Figure 5.5). In addition, 9/16 were adequate for experiments after lift-off and we could therefore proceed with wire bonding and characterisation of the microheaters. The other structures either suffered from incomplete lift-off (Figure 5.7b) or detached wires (Figure 5.8) making them inadequate for thermal characterisation. However, it is important to discuss the fabrication process for future work.

The two layers, the ASIs and the microheaters, are somewhat misaligned as can be seen from the four corners in Figure 5.4. Corner A is well aligned while the rest of the corners are misaligned. The misalignment of the four corners arises from a relative rotation of the coordinate system during the last exposure. It seems as though the coordinate system has rotated around A, meaning B would mainly shift in the vertical direction, C in the horizontal direction and D in both directions. This is very similar to the measured misalignment which are summarized in Figure 6.1. The rotational angles were calculated based on the misalignment in Table 5.2 and the design dimensions in appendix C. The measurements were done manually and some human error is expected. However, the angles are within the same range, supporting

that the misalignment occurs from a rotation of the coordinate system during the second exposure. The machine used for the exposure, Heidelberg MLA 150, has an internal setting which adjusts for the relative rotation. However, it seems like the setting might have either been deactivated or not good enough to completely compensate of the rotation of the sample.

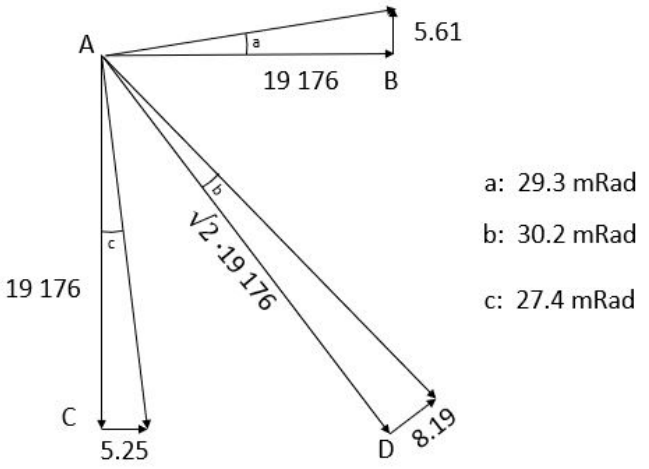

Figure 6.1: The displacement for the other corners relative to point A and the estimated rotational angle from each point. The dimensions are given in µm. Note that the dimensions of the lines and corners are not excact and are used as an illustration.

The wire widths and spacing of the design compared to the measurements obtained from Figure 5.6 are summarized in Table 6.1. The heater wire width (W_H) and thermometer wire width (W_T) are wider than the design with 0.4 µm and 1 µm. The increased wire widths are most likely because of the resist profile. Since SPR700 is a positive resist it often results in overcut resist profiles (Figure 3.6a) which will lead to wider structures as more resist than intended are solved [8]. However, this needs to be confirmed by obtaining a cross-section image of the resist profile. The thermometer exhibit the greatest relative error with 10%. However, the increased width will not change the function of the thermometer. The wire spacing is smaller than the design due to the increased wire widths but 14.5 µm is still an acceptable margin between the wires. Since the wire widths and spacing of the microheater were deemed acceptable and the ASIs were located inside of their intended area, the sample was ready for metalization.

Table 6.1: Designed parameters compared to measurements of the wire widths and spacing.

	W_H	W_T	Spacing
Designed	25.0	10.0	15.0
Measured	25.4	11.0	14.5

During lift-off, 9/16 microheaters had sufficient lift-off and could be used. The rest of the microheater either had damaged wires or incomplete lift-off resulting in inadequate microheaters.

Incomplete lift-off, as shown in Figure 5.2a, arises from gold adhering to the sidewalls or too short exposure in acetone. The gold adhering to sidewalls could be caused by an overcut resist profile (Figure 3.6a) which is often achieved with positive photoresist. If the resist profile is the reason it could be an option to switch to a negative resist which often results in an undercut resist profile (Figure 3.6c). The undercut profile reduces the amount of metal which is in contact with the sidewalls. The reduced contact between the sidewalls and the metal often increases the chance of complete lift-off. Positive photoresist was used in the previous fabrication method (Figure 4.2) to avoid involving HMDS since it was experienced better adhesion with SPR700. It initially succeeded to fabricate microheaters, making it natural to proceed with the same technique for creating new microheaters. However, since the fabrication process eventually

required HMDS for SPR700 it would be suitable to switch to a negative resist as it can increase the yield in lift-off. In addition, ultrasonic bath [25] could be used during lift-off to increase the chances of complete lift-off. It provides a stable acetone environment with sound vibrations which causes the resist to dissolve in controlled circumstances compared to showering the sample manually [25].

Three microheaters had detached heater wires, which is shown in Figure 5.8. Insufficient adhesion between the titanium and gold stack and the silicon wafer appears to be the problem during the lift-off process. The metalization was done in two seperate batches with identical settings (Table 4.1) and should therefore yield similar results. However, the three microheater which struggled with detached wires were metalized in the second batch. It is therefore reasonable to assume something went wrong during the second metalization as the two batches have disparate results from lift-off. One possible reason could be problems with the titanium layer during the second metalization as it is present to increase the adhesion between the gold and silicon wafer. Further analysis would involve comparing the cross-section images of two microheaters, one from each batch. It would be expected that the titanium layer in the second batch is uneven or not present at all if the problem is related to the titanium layer. In addition, the second batch was metalized two weeks after microheater resist structures were created and the sample could have attracted more contaminations. However, both processes involved plasma cleaning before metalization which would remove contaminations and ensure relatively equal adhesion properties before metalization.

6.4 Wire bonding

After metalization, the microheaters were divided into seperate pieces with scribing. Subsequently, wire bonding was necessary to connect a microheater to the chip-container for thermal characterization of the microheater.

The first wire bonding process required few attempts. Based on the connections given in Figure 5.9 it seems like the microheater and chip-container have a solid connection although this must be verified experimentally with electrical measurements. The second and third wire bonding required a lot of attempts as can be seen in Figure 5.10. Each hole represents one bonding attempt. The ball is able to form a connection at the contact pad but the connection detaches from the substrate when the capillary is lifted leaving behind holes. The problem seems to be poor adhesion between the titanium/gold stack and the silicon wafer as the gold is not sufficiently attached to the substrate.

All of the wire bonding processes used the same parameters (Table 4.4) and the microheaters were metalized with identical metalization configurations (Table 4.3) It would therefore be expected with consistent wire bonding results. However, the two batches showed inconsistent wire bonding. The only difference between the microheaters were their metalization batch. The two microheaters which required many attempts during wire bonding were from the second batch of metalization which had detached wires during lift-off, indicating poor adhesion. The hypothesis of poor adhesion between titanium/gold stack caused by the second metalization is strengthened.

6.5 Test chamber setup

In total three microheaters were wire bonded to the chip-container and attached to the test chamber. The pins connecting the test chamber to the chip-container (Figure 4.5c) were sensitive and at least one pin was not in contact in each experiment, ruining the setup for four point measurements. Therefore, only two point measurements of the thermometer resistance was performed. In addition, extensive force with tweezers had to be used to connect and remove the chip-container from the test chamber. The microheater wires are sensitive to contact with tweezers as wires can be destroyed and wire bonds can be dislocated, destroying the experiment.

To adjust for the sub-optimal setup it would be possible to use a squared stamp to carefully place the chip-container in test chamber. This would provide even force all over the chip-container and the chances of destroying wires or wire bonds are reduced compared to the use of tweezers. In addition, it would be possible to create a small circular hole in the test chamber where the chip-container is attached. The opposite end of the stamp could be used to remove the chip-container without using tweezers.

The test chamber was primarily made to provide control of the microheater such that current could be forced through the heater and the resistance of the thermometer could be obtained by four point measurements. In addition, it was attempted to create the structure such that it could be tested in the MOKE microscopy which required a lens being placed close to the ASIs. In the design process of the test chamber it was not focused on any height restrictions which evidently resulted in the destruction of the test chamber and conducting silver glue had to be used to analyze the ASIs in the MOKE microscope. In future production of test chambers, all the critical dimensions must be optimized so the system is compatible with the instrument used for analysing the ASIs.

6.6 Current sweep and MOKE microscopy

In total, two current sweeps were performed. The first sweep burned the microheater as seen in Figure 5.11a. The high temperature seemed to oxidize the microheater, destroying the electrical contact as it was not possible to force current through it. Chemical interactions resulted in contaminations on the heater wires and were most likely caused by the high temperature. In addition, the wires appear to be damaged in Figure 5.11a. The damage was probably caused by removing the chip-container from the test chamber as this required extensive force with tweezers. The current sweep was swept from 0 A to 1A which is a high current for a gold thin film and in retrospect, the current should have been lower.

The second current sweep was performed on another microheater with several step functions within the current range 0 mA to 40 mA (Figure 5.12b). The measured thermometer resistance is shown in Figure 5.12a and it has eight clearly distinguishable levels. However, as can be seen in Figure 5.12b there are nine major current shifts. The first major step function from 1 mA to 10 mA results in a small change in the resistance. The ohmic heating before 10mA is therefore not sufficient to noticeably increase the temperature above room temperature.

The heat generated by ohmic heating is $P = R \cdot I^2$ and the temperature should therefore be linear with I^2. This assumes that the power contribution from the temperature change in the heater resistance is relatively small. Region 0, 1 and 2 stabilizes to a constant level in Figure 5.12a but region 3 keeps in increasing and does not stabilize within the time of the measurement. The average resistances of the final 30 seconds were calculated for region 0, 1 and 2, while only 8 seconds were used in region 3 because of the slow settling. The resistance for region 3 is therefore a bit lower than the final value would be if the system had time to reach an equilibrium. The temperatures were obtained with eq. (3.1) by inserting $T_0 = 18°\text{C}$ and the measured thermometer resistance $R(T_0) = 140.8\Omega$. Based on the estimated temperatures and the heater currents, the temperature and current relation is given in Figure 6.2. This shows that the temperature increases linearly with the square of the current and therefore also the power generated by the heater.

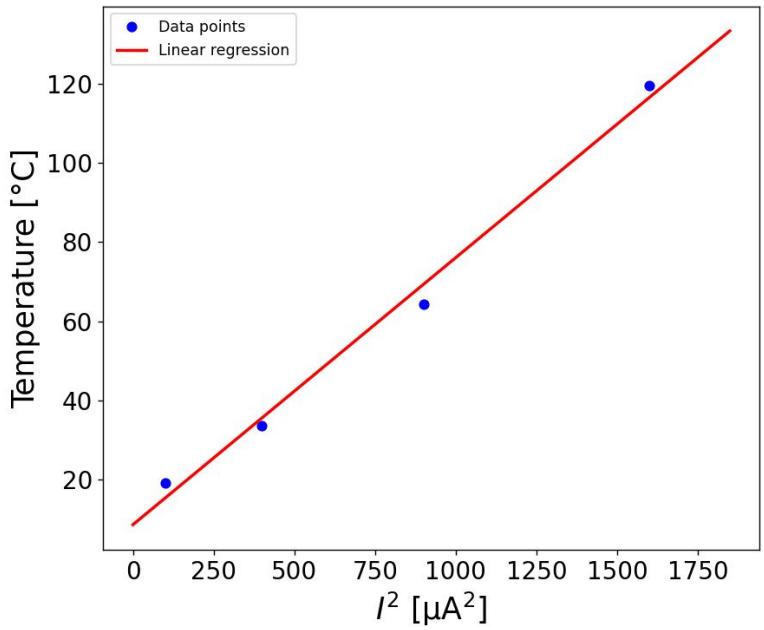

Figure 6.2: The data points used to create the linear regression displaying the relation between the temperature of the thermometer and the square of the heater current.

When the heater current is adjusted using step functions as shown in Figure 5.12b, it takes time for the substrate to reach an equilibrium. The process of approaching the equilibrium is evident in Figure 5.12a since the resistance increases linearly with substrate temperature, as shown in Figure 5.3. The substrates temperature exhibits the exponential settling characteristic of a heating system controlled by a time constant [10]. The various settling times can be explained by the increased temperature steps in the regions 1,2 and 3 in Figure 5.12a. The time constant is influenced by factors such as the temperature of the surroundings, the heat capacity of the substrate, and the thermal conductivity of the materials involved [10]. The disparity between the settling values for the same heater currents proves that the system did not settle properly and if the current remains constant for a long time, eventually it will settle to the same value, independent of the previous temperature.

The temperature coefficient of metals are only linear locally, e.g., within certain temperature ranges. Therefore the exact temperature generated from the heater will have a greater error further away from the last confirmed temperature measurement used in the calibration for the temperature coefficient, which in our case is 130°C. The maximum temperature should be around 130°C if the experiment requires high precision. As previously mentioned, it was not possible to perform four point measurements for the calibrations of the microheater and the thermometer resistance. The data obtained is therefore less precise since two point sensing includes the contact resistance. If the system were to be used for high accuracy measurements, being able to make four point measurements is necessary for precise temperature control.

The microheater has been thoroughly characterized and the system could be placed in the MOKE microscope. However, no magnetic contrast was observed. The insufficient magnetic contrast most likely occurs from oxidation of the nanomagnets. Firstly, the nanomagnets, being 10 nm thick, are susceptible to oxidation as the Al only protects the top parts of the nanomagnets, leaving the sides exposed. Secondly, the exposure of nanomagnets to elevated temperatures can accelerate the oxidation process. In addition, delayed analysis of the ASIs after production allows sufficient time for oxidation to occur.

Chapter 7

Conclusion and future work

In this thesis, we have successfully fabricated and validated an on-chip microheater surrounding ASIs. The increased temperature is generated by the heater current and thermal conduction increases the substrate temperature due to the temperature gradient. The generated temperature is determined by measuring the resistance of the thermometer and utilizing the locally constant temperature coefficient for metals. The microheater was realized using photolitography and metalization. During the fabrication we encountered adhesion problems between the silicon wafer and the positive photoresist SPR700 but applying HMDS solved the problem. We metalized the microheaters with 5 nm layer of titanium followed by a 145 nm layer of either gold or copper. Subsequently, we estimated the temperature coefficients for two microheaters. The temperature coefficients were found to be $\alpha_{Gold} = 2.51$ mΩ/°C and $\alpha_{Copper} = 2.98$ mΩ/°C , aligning with the expected trend of $\alpha_{Gold} < \alpha_{Copper}$, as observed in bulk materials ($\alpha_{Gold} = 3.72$ mΩ/°C $< \alpha_{Copper} = 4.04$ mΩ/°C). To test the microheater, a current sweep through the heater from 0 mA to 40 mA was done. The current sweep involved several step functions and showed an expected transient response for the substrate temperature before the system stabilized. An average of the stabilized resistance values at each current level was calculated and the corresponding temperature, using the temperature coefficients, was obtained. Subsequently, it was proved that the temperature is linear with the square of the current, aligning with the heat generated from ohmic heating ($P = R \cdot I^2$). The microheater is capable of providing accurate temperatures up to 130°C for ASIs. Insufficient planning of the test chamber resulted in adjustments requiring conducting silver glue to analyze the magnetic contrast by MOKE microscopy. When analyzing the ASIs we encountered insufficient magnetic contrast, rendering the experiment inconclusive, most likely due to oxidation of the nanomagnets.

Some challenges were faced in the thermal characterisation, such as absence of connection between the test chamber and the chip-container. In addition, the removing the chip-container from the test chamber by tweezers destroyed three experiments. The microheaters containing ASIs were metalized in seperate batches and the second batch encountered adhesion problems during lift-off and wire bonding, indicating that something went wrong in the second metalization.

However, the microheater was fabricated and validated through thermal characterisation. In addition, the test chamber provided a system capable of controlling the temperature of ASIs. The fabrication technique of the microheaters and the thermal control provided by the test chamber have the potential to be utilized in future analysis of ASIs.

For future work it would be valuable to develop a system capable of providing temperature control in real time by using feedback to regulate the heater current. In order to design a feedback system that provides precise real-time control of the heating, it is essential to further analyze both transient and steady-state heating. In addition, experimenting with different heater wire widths and wire spacing would also reveal more about the microheater potential such that the microheater can be altered after the required heating conditions for the ASIs used in the experiment. Finally, the test chamber controlling the microheater needs to be adjusted carefully and designed such that it is compatible with the instruments used during analysis of ASIs.

Appendix A

Design microheater 1

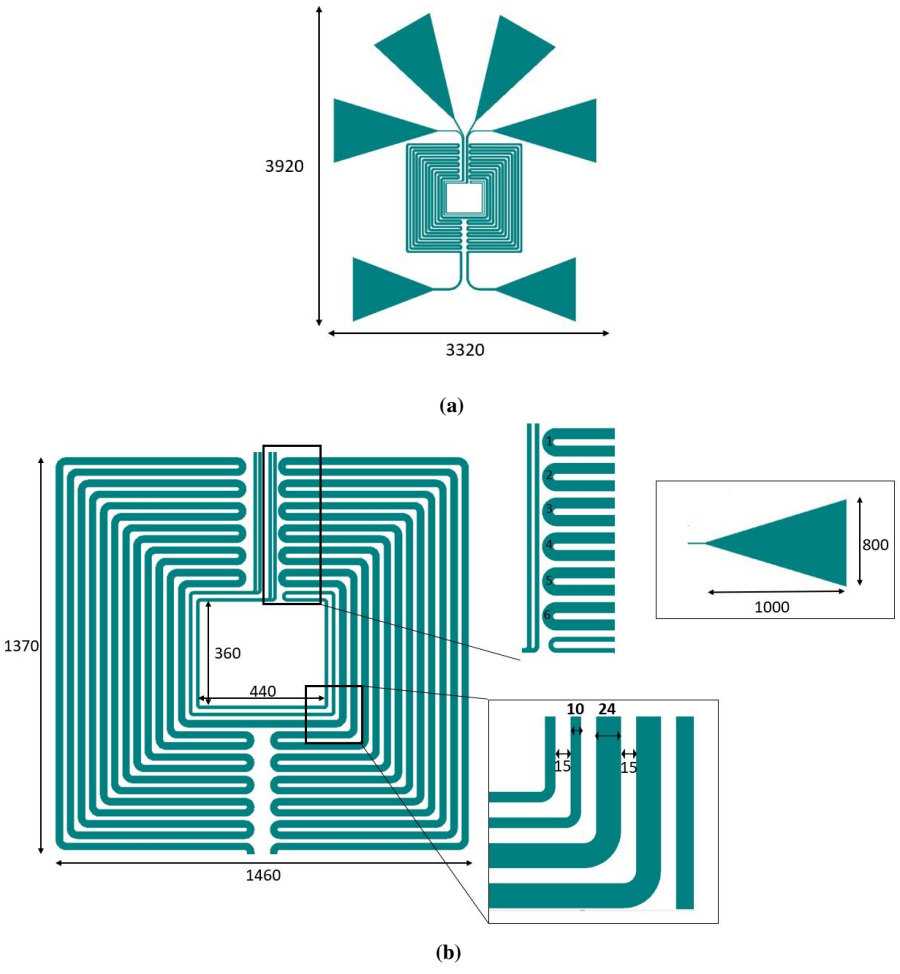

Figure A.1: The design of the microheater with dimensions given in µm with a) an overview and b) a detailed image of the microheater.

Appendix B

ASI design

Area 1 and 3 consists of square ice structures while area 2 and 4 consists of the pinwheel structure. Area 1 and 2 have varying the pitches 300 nm, 320 nm, 360 nm and 400 nm while area 3 and 4 have the pitches 300 nm, 320 nm, 340 nm, 360 nm, 380 nm, 400 nm and 440 nm from left to right.

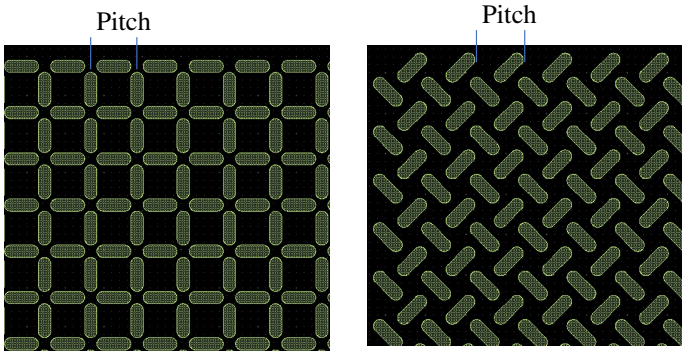

(a)

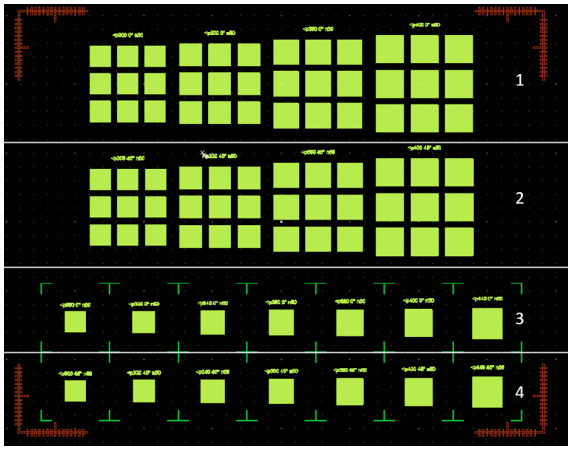

(b)

Figure B.1: a) The left structure is the square ice and the right is the pinwheel ice. b) The total nanomagnet structure. Area 1 and 3 consists of square ice structures with varying pitch while area 2 and 4 consists of pinwheel geometries with varying pitch.

Appendix C

Design microheater 2

Minor changes have been performed on this design which involves the wire spacing of the four wires emerging out of the heater due to small spacing in the previous design. The heater wire widths increased with $1\,\mu\mathrm{m}$ and only consists of five windings. These changes were done in the attempt to align the alignment marks for the ASIs and the microheater.

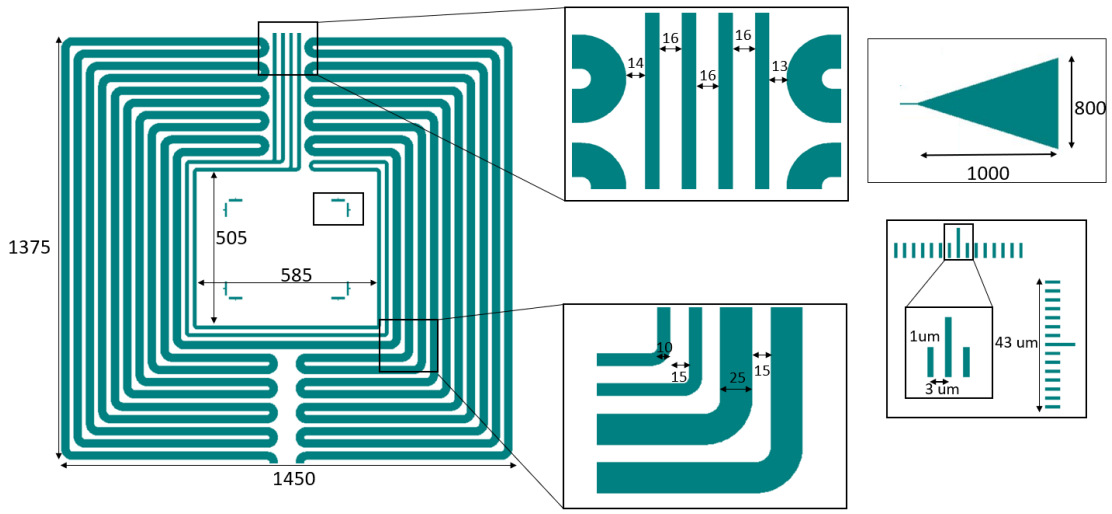

(a)

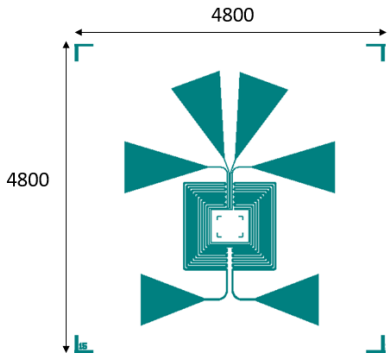

(b)

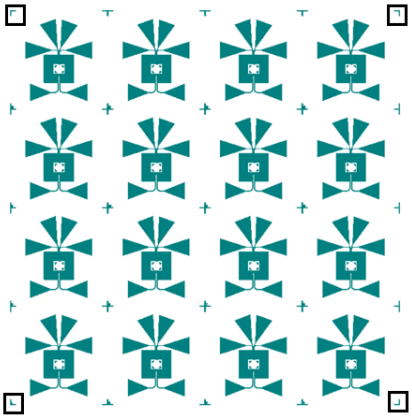

(c)

Figure C.1: a) Zoomed image of the heater, thermometer, spacing, alignment marks and pad dimensions. b) Total structure with dies. c) The alignment marks used during the exposure of the microheater patterns.

Appendix D

Thermal calibration data

Table D.1: Gold data for linear regression.

Temp	Mean[Ω]	Std[mΩ]
30	90.43	54
50	94.99	82
64	98.53	90
80	102.52	115
100	106.28	102
130	112.7	136

Table D.2: Copper data for linear regression.

Temp	Mean[Ω]	Std[mΩ]
25	112.81	29
35	115.83	89
45	118.21	67
60	122.52	114
75	127.03	99
89	131.75	175
105	136.33	322
130	142.83	293

Appendix E

Custom made test chamber

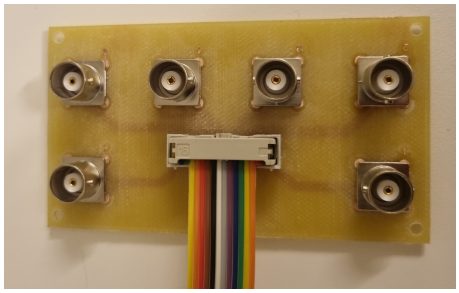

(a)

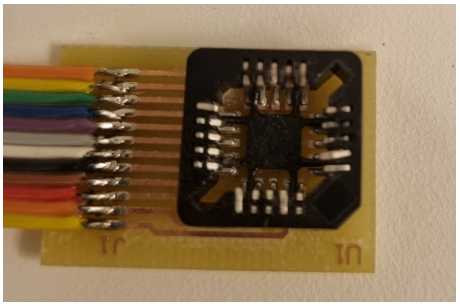

(b)

Figure E.1: a) Coaxial signals capable of connecting the system to SMUs. b) Test chamber meant for the chip-container providing electrical contact between the coaxial signals and the microheater.

Bibliography

[1] J. Jensen et al. Computation in artificial spin ice. *MIT Press*, 31, 2018. DOI: https://doi.org/10.1162/isal_a_00011.

[2] Porro et al. Magnetization dynamics of weakly interacting sub-100 nm square artificial spin ices. *Scientific reports*, 9(1):19967, 2019. DOI:https://doi.org/10.1038/s41598-019-56219-y.

[3] S. Skjærvø et al. Advances in artificial spin ice. *Nature Reviews Physics*, 2(1):13–28, 2020. DOI: https://doi.org/10.1038/s42254-020-0148-x.

[4] M. Waldrop. The chips are down for moore's law. *Nature*, pages 144–147, 2 2016. DOI: 10.1038/530144a.

[5] L. Zhang et al. The challenges of modern computing and new opportunities for optics. *PhotoniX*, 9 2021. DOI: https://doi.org/10.1186/s43074-021-00042-0.

[6] C. Kittel. *Introduction to Solid State Physics*. Wiley, 8th edition, 2004. ISBN: 978-0-471-41526-8.

[7] A. Auerbach. *Interacting electrons and quantum magnetism*. Graduate texts in contemporary physics. Springer-Verlag, 1st edition, 1994. ISBN: 978-1-4612-6928-1.

[8] B. El-Kareh. *Fundamentals of Semiconductor Processing Technology*. Springer New York, NY, 1st edition, 2003. ISBN: 978-1-4613-5927-2.

[9] Theodor L. Bergman et al. *Fundamentals of Heat and Mass Transfer, 8th Edition*. Wiley, 8th edition, 2011. ISBN: 978-1-119-35388-1.

[10] A. Saggion. *Thermodynamics*. Springer, 1 edition, 2020. ISBN: 978-3-030-26975-3.

[11] Hugh Young and Roger Freedman. *Sears and Zemansky's University Physics with Modern Physics*. Pearson Education, 13th edition, 2011. ISBN:978-0-1351-5955-2.

[12] A. Ziabari et al. Adaptive power blurring techniques to calculate ic temperature profile under large temperature variations. *IEEE Transactions on Components, Packaging and Manufacturing Technology*, 2021.

[13] Graczykowski et al. Thermal conductivity and air-mediated losses in periodic porous silicon membranes at high temperatures. *Nature communications*, 8(1):415, 2017. DOI:https://doi.org/10.1038/s41467-017-00115-4.

[14] Kuphaldt and Tony R. Lessons in electric circuits, volume i–dc. *Vol Fifth Edition Open Book Project*, 2006. ISBN:978-1-9076-5307-0.

[15] P. Chauhan et al. *Copper Wire Bonding*. Springer-Verlag New York, 1st edition, 2014. ISBN: 978-1-4939-5349-3.

[16] D. Glocker and S. Shah. *Handbook of Thin Film Process Technology*. Taylor Francis Ltd, 2001. ISBN: 978-0-7503-0832-8.

[17] Mla 150. URL: https://heidelberg-instruments.com/wp-content/uploads/2021/10/fact-sheet-MLA150.pdf.

[18] Kim D. et al. Extreme anti-reflection enhanced magneto-optic kerr effect microscopy. 2020. DOI:https://doi.org/10.1038/s41467-020-19724-7.

[19] S. Morley et al. Thermally and feld-driven mobility of emergent magnetic charges in square artifcial spin ice. *Scientific reports*, 11 2019. DOI: https://doi.org/10.1038/s41598-019-52460-7.

[20] Phidl documentation. 09 2022. URL: https://phidl.readthedocs.io/en/latest/index.html.

[21] megaposit spr700 series photoresist. 5 2004. URL: https://scholvin.scripts.mit.edu /nano/Documents/resists.SPR700_Photoresist.pdf.

[22] Dinesh R. et al. Chapter 8 - Fundamentals and Applications of Plasma Cleaning. In Rajiv Kohli and K. L. Mittal, editors, *Developments in Surface Contamination and Cleaning: Applications of Cleaning Techniques*, pages 289–353. Elsevier, 2019. ISBN:978-0-12-815577-6.

[23] I.W. Selesnick and C.S. Burrus. Generalized digital butterworth filter design. *IEEE Transactions on Signal Processing*, 46(6):1688–1694, 1998. DOI=https://ieeexplore.ieee.org/document/678493.

[24] S.R. Syrtsov et al. Positive temperature coefficient of resistivity in thin films of barium titanate. *Materials Science in Semiconductor Processing*, 5(2):223–225, 2002. DOI: https://doi.org/10.1016/S1369-8001(02)00077-X.

[25] Mineo Ueki and Yoshiaki Mimura. Ultrasonic treatment applied to high quality lift-off technique. *Japanese Journal of Applied Physics*, 25(S1):165, 1986. DOI:https://iopscience.iop.org/article/10.7567/JJAPS.25S1.165.

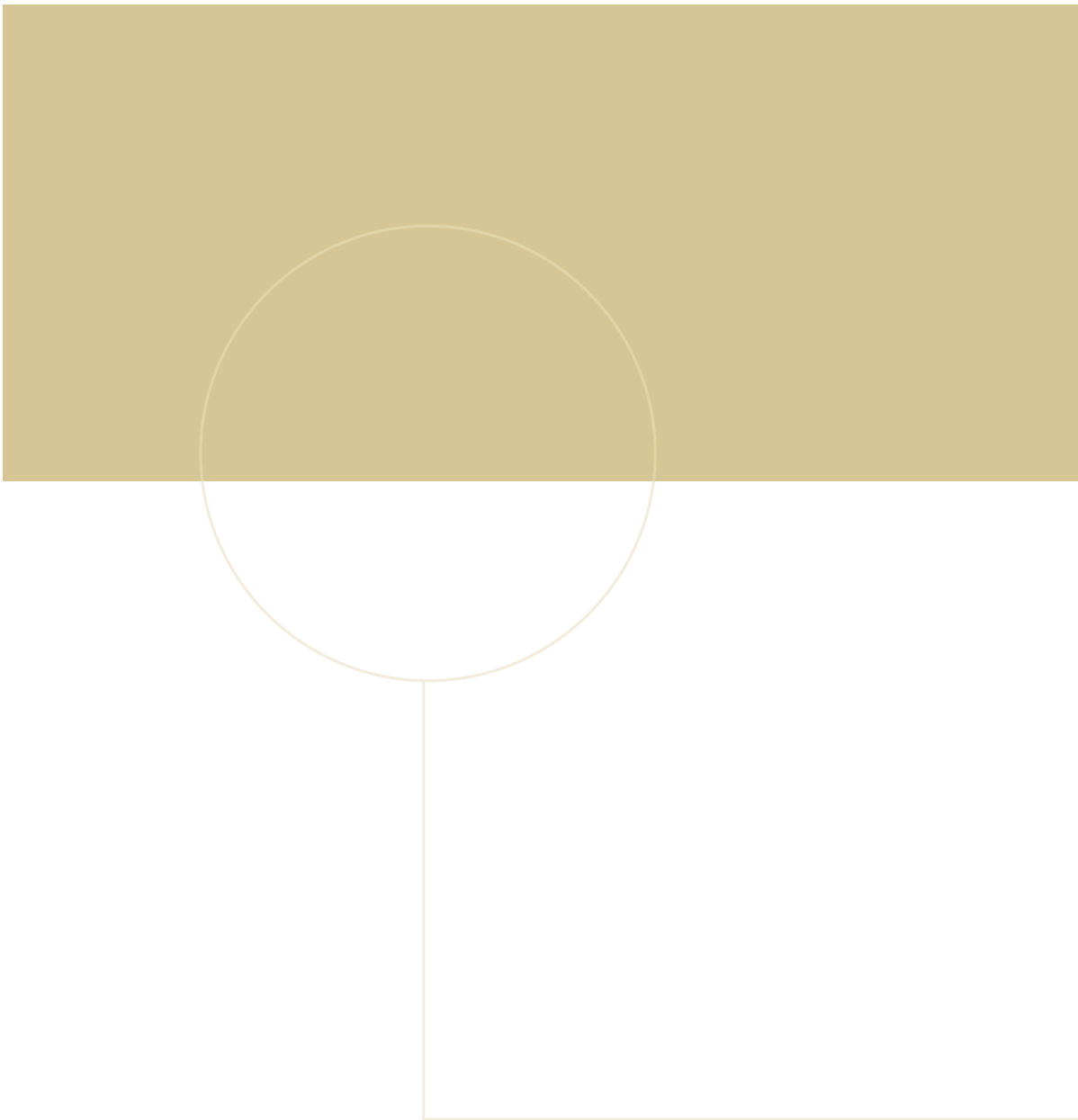

NTNU

Norwegian University of
Science and Technology